Effects of silver and strontium ions co-implanted into silicon carbide

by

Nqophisa Mtshonisi

Submitted in partial fulfilment of the requirements for the degree

Masters of Science (MSc) in Physics

In the faculty of Natural and Agricultural Sciences

University of Pretoria

Pretoria

December 2020

Supervisor: Prof T.T. Hlatshwayo

Co-supervisor: Dr. M Mlambo

DECLARATION OF ORIGINALITY

I, Nqophisa Mtshonisi declare that the dissertation, which I hereby submit for the degree of MSc in Physics at the University of Pretoria, is my own work and has not previously been submitted by me for a degree at this or any other tertiary university.

SIGNITURE: ………………………………………………

DATE: ………………………………………………………

UNIVERSITEIT VAN PRETORIA
UNIVERSITY OF PRETORIA
YUNIBESITHI YA PRETORIA

Summary

Effects of silver and strontium ions co-implanted into silicon carbide

BY

NQOPHISA MTSHONISI

Submitted in partial fulfilment of the requirements for the degree of MSc in Physics in the Faculty of Natural and Agricultural Science, University of Pretoria

Supervisor: Prof T.T. Hlatshwayo

Co-supervisor: Dr. M. Mlambo

In modern nuclear reactors safety is improved by cladding the fuel kernel with chemical vapor deposited layers of pyrolytic carbon and silicon carbide. Amid these cladding layers SiC is the primary diffusion barrier of radioactive fission products. During normal operations at about 900 ℃ to 1250 ℃, the coated fuel particle retains almost all the radioactive fission products excluding silver (Ag), strontium (Sr) and europium (Eu). Substantial research has been studied on the migration behavior of Ag in SiC while limited work has been done on the migration behavior of Sr and Eu in SiC. Moreover, less is known on the migration behavior of Ag in the presence of other important radioactive fission products in SiC.

In this study, the effects of Ag and Sr co-implanted into polycrystalline SiC were studied. 360 keV of Ag and Sr ions were individually implanted into polycrystalline SiC, both to a fluence of $2 \times 10^{16}\ cm^{-2}$ at 600 ℃ (Ag-SiC and Sr-SiC). Some of the Ag-SiC samples were then implanted with 280 keV Sr ions to a fluence of $2 \times 10^{16}\ cm^{-2}$ at 600 ℃ (Ag&Sr-SiC). This high temperature of implantation was chosen to maintain the crystallinity of the substrate and also the modern nuclear reactors are premeditated to function at elevated temperatures.

The implanted samples were isochronally annealed at temperatures varying from 1000 ℃ to 1400 ℃ in steps of 100 ℃ for 5 hours. Structural and surface morphological evaluations were monitored by Raman spectroscopy and scanning electron microscopy (SEM) while the migration behavior of implanted species were monitored by Rutherford backscattered spectrometry (RBS).

Both individual and co-implantations retained crystallinity of polycrystalline-SiC with some defects. More defects were observed in the co-implanted samples. Annealing the samples caused progressive annealing of defects and appearance of SiC crystallites on the surface. These crystallites grew with annealing temperature and their growth was enhanced in the samples implanted with Ag. Neither migration nor loss of Sr were observed in Sr-SiC samples throughout the annealing steps. While annealing the Ag-SiC and Ag&Sr-SiC samples affected implants to shift towards the surface accompanied by loss at temperatures above 1400 ℃. Hence the presence of Ag has role in the migration and the loss of the implanted species.

Acknowledgements

Be strong and of great courage, don't fear nor be anxious of them; for the Lord your GOD, He is the One who goes with you. He will not take off you nor spurn you. Deuteronomy 31:6

Working on my MSc dissertation has been a superb and overwhelming experience. Without the assistance of numerous individuals to overcome the issues would not be conceivable. I am obliged to numerous individuals making the time working on my MSc an episode to remember. I would like to say my thanks to the following:

My most profound appreciation to my supervisor Prof TT Hlatshwayo as well as to my co-supervisor Dr. M Mlambo. With my deepest gratitude I'd like to thank their patience, vision and their sacrifice to my work in addition to their friendly and interactive approach was of great importance. Without their tireless efforts, determination, positive attitude and constructive ideas which is greatly appreciated, it would be impossible for me to complete my dissertation. Above all, I thank them for funding me on my MSc.

My work has incredibly profited from discussions, suggestions and support from my nuclear material group members. I wish to thank all my group members, it has been a privilege to get to know you and collaborate with all of you. I learnt a lot from you especially how to work with different equipment.

Finally, my family and friends that have the same vision and always encouraged me to do my best and constantly checking up on me, supporting and loving me.

List of Figures

Figure 1.1: *An illustration of the Pebble Bed TRISO fuel sphere cross-section-------------------11*

Figure 1.2: *Tetrahedron showing (a) one carbon bonded to 4 silicon atoms and (b) one silicon bonded to 4 carbon atoms---13*

Figure 1.3: *The stacking sequence for SiC polytypes in the 1120 plane. (a) 2H-, (b) 4H-, (c) 6H-, (d) 15R- and (e) 3C-SiC---14*

Figure 2.1: *Schematic representation of the vacancy diffusion mechanism. The empty space represents the vacancy and the grey and black circles represents atoms. (a) and (b) shows the positions before and after diffusion respectively---23*

Figure 2.2: *Interstitial mechanism (a) before and (b) after an interstitial diffusion---------------24*

Figure 2.2: *Illustration of (a) polycrystalline and (b) single crystalline----------------------------25*

Figure 3.1: *The nuclear and electronic stopping power as a function of ion energy-------------28*

Figure 3.2: *A typical nuclear elastic collision between the initial momentum of M_1 and stationary target atom of M_2 and the final momentum of the M_1 and M_2--30*

Figure 3.2: *Illustration of the path of a single ion travelling inside a solid target at an angle not equal to the surface normal until it reaches a certain depth within the solid target----------------35*

Figure 4.1: *Typical Raman spectrum of virgin SiC obtained in the Raman spectroscopy laboratory at University of Pretoria---39*

Figure 4.2*: Diagram of Rayleigh and Raman scattering process-----------------------------------41*

Figure 4.3: *Image of Raman spectroscopy at the University of Pretoria----------------------------43*

Figure 4.4: *Illustration of an ion beam accelerated towards the material-------------------------44*

Figure 4.5*: (A) a schematic representation of a Van de Graaff accelerator and (B) radio-frequency ion source--46*

Figure 4.6: *A block diagram for the RBS chamber circuit---47*

Figure 4.7: *The spectrum of polycrystalline-SiC co-implanted with silver and strontium, with arrows indicate the surface positions of the elements*--48

Figure 4.8: *Schematic picture of elastic scattering.* M_1 *and* M_2 *are the masses of the incident ion and recoiling atoms, respectively*---49

Figure 4.9: *A schematic diagram illustrating the backscattering event of particles and energy loss from depth x*---52

Figure 4.10: *The interaction of electron beam with specimen and the signal emitted from the sample*---56

Figure 4.11: *Show the FEG-SEM at the University of Pretoria*-------------------------------------57

Figure 6.1: *SRIM 2013 simulated depth profiles and displacement per atom (dpa) of (a) Ag (360 keV) & Sr (280keV) and (b) Sr (360 keV) implanted into SiC*--64

Figure 6.2: *Raman spectra of (a) un-implanted SiC and (b) individual and co-implanted SiC (Ag-SiC, Sr-SiC and Ag&Sr-SiC)* ---65

Figure 6.3: *Raman spectra of the annealed (a) Ag-SiC, (b) Sr-SiC and (c) Ag&Sr-SiC at* $1000\ ℃, 1200\ ℃\ and\ 1400\ ℃$---67

Figure 6.4: *The full width at half maximum (FWHM) of LO mode of Ag-SiC, Sr-SiC and Ag&Sr-SiC as function of annealing temperature*--68

Figure 6.5: *SEM micrographs of as-received SiC, Ag-SiC, Sr-SiC and Ag&Sr-SiC samples*----69

Figure 6.6: *SEM micrographs of Ag-SiC, Sr-SiC and Ag&Sr-SiC sequentially annealed from* $1000-1400℃$ *in steps of* $100℃$ *for 5 hours*--70

Figure 6.7: *Rutherford backscattering spectrometry spectra of (a) Ag-SiC, (b) Sr-SiC, and (c) Ag&Sr-SiC. The arrows indicate the surface position of elements*-----------------------------------71

Figure 6.8: *(a) Ag-SiC, (b) Sr-SiC and (c) Ag&Sr-SiC. The as-implanted and then sequential annealed from* $1000\ ℃\ to\ 1400\ ℃$ *in steps of* $100\ ℃$ *for 5 hours*-----------------------------------73

Figure 6.9: *Retained ratio and peak position of implants of Ag-SiC, Sr-SiC and Ag&Sr-SiC samples before and after sequential annealing at temperatures from* 1000 ℃ *to* 1400 ℃ *in steps of* 100 ℃ *for 5 hours*---74

List of Tables

Table 4.1: *Table showing the Kinematic factor* k *of different target atoms at a scattering angle θ= 165 ° and the backscattered energy*---50

Table 6.1: *Shows the full with at half maximum of the polycrystalline SiC virgin and as-implanted of Ag-SiC, Sr-SiC and Ag&Sr-SiC*---66

Table 6.2: *Showing the peak intensities of the annealed samples of Ag-SiC, Sr-SiC and Ag&Sr-SiC at* 1000 ℃, 1200 ℃ and 1400 ℃---67

Table of Contents

Summary i

Acknowledgements iii

List of Figures .... **Error! Bookmark not defined.**

List of Tables vi

Chapter 1: Introduction 10

1.1 Background 10

1.2 Silicon Carbide (SiC) 12

1.2.1 Lattice structure of SiC 12

1.3 Previous studies of Ag and Sr migration behavior in SiC 15

1.4 Motivation of this study 16

1.5 Outlay of the Dissertation 17

References 18

Chapter 2: Diffusion 22

2.1 Diffusion mathematics 22

2.2 Mechanism of diffusion in solids 23

2.2.1 Vacancy mechanism 23

2.1.2 Interstitial mechanism 24

2.1.3 Dislocation and Grain boundary 24

2.3 Diffusion in polycrystalline SiC 24

2.4 Evaluation of the diffusion coefficient 25

References 26

Chapter 3: Ion implantation 27

3.1 Stopping power 27

3.1.1 Nuclear stopping 29

3.1.2 Electronic stopping 31

3.2 Energy loss in compounds 32

3.3 Energy straggling 33

3.4 Range and Range straggling 33

3.5 Stopping and Range of Ions in Matter (SRIM) for simulation of ion implantation 36

References 37

Chapter 4: Experimental-analysis techniques 39

4.1 Raman spectroscopy 39

4.1.1 Detection and analysis of inelastic scattered radiation 39

4.1.2 Raman Effect 41

4.1.3 Raman spectroscopy experimental setup 43

4.2 Rutherford Backscattering Spectrometry 43

4.2.1 Components of the Rutherford back scattering spectrometry 44

4.2.2 Kinematic Factor 48

4.2.3 Differential cross section 50

4.2.4 Depth profiling 51

4.3 Scanning electron microscopy (SEM) 53

4.3.2 Fundamental principles of SEM 54

4.3.3 Instrumentation 56

References 58

Chapter 5: Experimental procedure 61

5.1 Sample preparation 61

5.2 Implantation 61

5.3 Annealing of the samples 61

5.4 Raman spectroscopy, SEM and RBS measurement conditions 62

CHAPTER 6: Results and Discussion 63

6.1 Simulation results 63

6.2 Raman results 64

6.3 SEM results 68

6.4 RBS results 70

Chapter 7: Conclusion and future work 77

Chapter 8: Appendix 79

8.1 A publication in peer reviewed journal 79

8.2 Conference presentation 79

Chapter 1: Introduction

1.1 Background

Scientific evidence has shown that slackening climate change revolves around technological advances geared in improving and using clean sources of energy [1]. There are four methods of generate electricity: fossil, hydro, renewable and nuclear. In fossil fuel method, the hydrocarbons such as coal, oil or natural gas are burnt-out to produce energy in the form of heat. This heat is then utilized to boil water which produces steam that drives the turbines to produce electricity. However, by burning hydrocarbon fuels, large quantities of carbon dioxide are produced, which is one of the greenhouse gasses that contribute to climate change [2]. In hydro method, the energy is generated by stowing water in huge reservoirs behind gigantic dams. Water is released from the reservoir and streams through a turbine, spinning the turbine which in turn enables a generator to produce electricity. However, in dry periods the production of electricity can deplete these reservoirs. The overflowing of reservoirs behind dams in wet seasons, and the abating of the stream of the river can have a genuine negative affect on the ecology of the region around the dams. Furthermore, there are only a limited number of sites suitable for new dams [3]. In renewable method, energy is generated using natural resources to produce electricity, but renewable energy does not usually produce electricity at a constant and reliable basis. For example, the amount of electricity generated by wind turbines fluctuates with wind speed; in the event that the wind is as well powerless or as well solid at that point no electricity can be generated. Solar panels depend on the quality of the daylight, which depends on the time of day and the amount of cloud cover. Hence renewable energy is not reliable sources of energy [3].

Each form of electricity generation method has its qualities and shortcomings, however, long term electricity generation must produce low amounts of greenhouse gas emissions. Nuclear energy gives reliable supplies of electricity, with no carbon emissions and moderately small amounts of waste that can be securely put away and inevitably disposed [4]. Nuclear reactors can play a vital part in assembly the world's ever-increasing demands of clean and reasonable energy [5]. Nuclear generating power plants can operate for over 60 years. This means that the economy of nuclear energy generation depends on its capacity to produce vast and uninterrupted amounts of electricity

for a long time with stable electricity costs. Against the great records of environmental friendly electricity generation, subsequently stands the fear of a disastrous nuclear accident.

In the modern high temperature gas-cooled reactors (HTGRs) like the pebble bed modular reactor (PBMR), safety is improved by coating the fuel kernel with carbon and silicon carbide layers. The typical PBMR coated particle is demonstrated in Figure 1.1 [6]. The fuel particle comprises of an inner uranium dioxide core with a diameter 0.5 mm surrounded by four successive chemical vapor deposition (CVD) layers [7]. These are: 95 μm inner layer porous graphite buffer layer, 40 μm inner pyrolytic carbon (IPyC), 35 μm silicon carbide (SiC) and 40 μm outer pyrolytic carbon (OPyC) layers [8,9,10]. This coated particle is about 0.92 mm in diameter. The porous carbon buffer layer accommodates the change in volume and density of the kernel [10]. IPyC layer acts as a dissemination boundary for non-metallic fission products (FPs). SiC layer acts as the diffusion barrier for metallic FPs. Additionally, SiC layer gives adequate structural steadiness amid compact fabrication [7-11]. The OPyC layer cover the SiC layer and protects it from tensile stress. The coated particle is identified as the tri-structural isotropic (TRISO) fuel particle [12]. The PBMR fuel is made up of approximately 15000 of these TRISO particles that are embedded in the 60 mm graphite matrix.

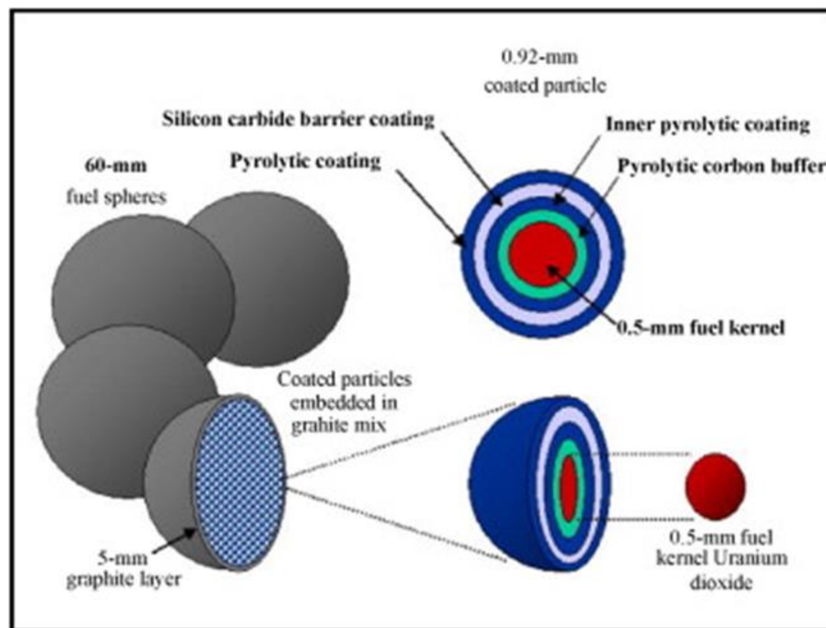

Figure 1.4: *An illustration of the Pebble Bed TRISO fuel sphere cross-section. Taken from Donald Gee [6].*

In a nuclear reactor, a thermal neutron reacts with ^{235}U (uranium) isotope to produce an unstable ^{236}U. ^{236}U splits or fissions into two different light nuclei called fission products (FPs); 3 neutrons and a sum of energy is released. The 3 new neutrons are permitted to react with ^{235}U resulting in a chain reaction. Thus, neutrons are required to sustain the chain reaction. The heat release amid fission is then transferred into a steam generator by coolant to produce electricity.

Some of FPs are radioactive and need to be kept in the fuel. The release rates of FPs by TRISO particle during normal operations at about 900 ℃ to 1250 ℃ is very low [13]. Under the operation conditions the TRISO particle retains almost all the important FPs such as: iodine (I), cesium (Ce), krypton (Kr) and xenon (Xe) with the exclusion of silver (Ag) and strontium (Sr) [11, 12].

The release of FPs to environment can lead to various health hazards. ^{110m}Ag is a strong gamma (γ) radiation emitter with relatively long half-life of 253 days [12,14], and is produced through neutron capture by ^{109}Ag. ^{109}Ag is a stable isotope of low fission yield (approximately 0.03 % for ^{235}U [6]) and its low transformation rate of ordinarily 0.1 % of ^{109}Ag to ^{110m}Ag by neutron capture. ^{110m}Ag can cause genuine issues within the reactor due to its high vapor pressure which might contaminate the cooling gas pumps and heat exchangers within the cooling circuit. ^{90}Sr is a radioactive isotope of ^{89}Sr produced by nuclear fission, with a half-life of 26.5 years [7,10]. Radioactive ^{90}Sr can be released from nuclear weapons and/or during nuclear accidents. When ^{90}Sr is absorbed in food and water it can create health concerns. It exhibits similar biochemical behavior to calcium and can replace calcium in the bone and teeth thereby causing cancers of the bone and bone marrow [15].

1.2 Silicon Carbide (SiC)

1.2.1 Lattice structure of SiC

As mentioned earlier, SiC layer is the main barrier of FPs because of its ability to maintain its properties at elevated temperatures. SiC is one of the hardest materials because of its strentgth between Si and C. For all polytypes the distance between the neighboring Si and C atoms is about 1.89 Ǻ [16] and the distance between the neighboring C and C atom is about 3.08 Ǻ [17]. Some of SiC properties include: resistance against chemical and abrasive attacks, high thermal conductivity, high temperature stability and radiation resistance. Additionally, SiC is utilized in

high temperatures, high power, electronic gadgets, light emitters and radiation detectors for energetic ions [7]. SiC is the proposed material for future nuclear reactors as Si and C have low neutron absorption cross sections. The core of the TRISO fuel particle does not exceed 1600 ℃, in case of core heat up occurrences, SiC sublimates at temperatures about 2800 ℃. Howbeit, some researchers have noted that SiC starts to decompose at 1500 ℃ into Si, C, SiC_2 and Si_2C [18,19]. In a TRISO fuel particle the 3C-SiC (β) layer is preferred for nuclear reactors due to its higher radiation resistance against neutron bombardment than the alpha-SiC [7,20].

SiC is a covalently bonded tetrahedron that can take either of the two forms; SiC_4 or CSi_4. Si is the center bonded to 4 carbons atoms or C is the center bonded to 4 silicon atoms and θ is a bond angle between the two atoms [7].

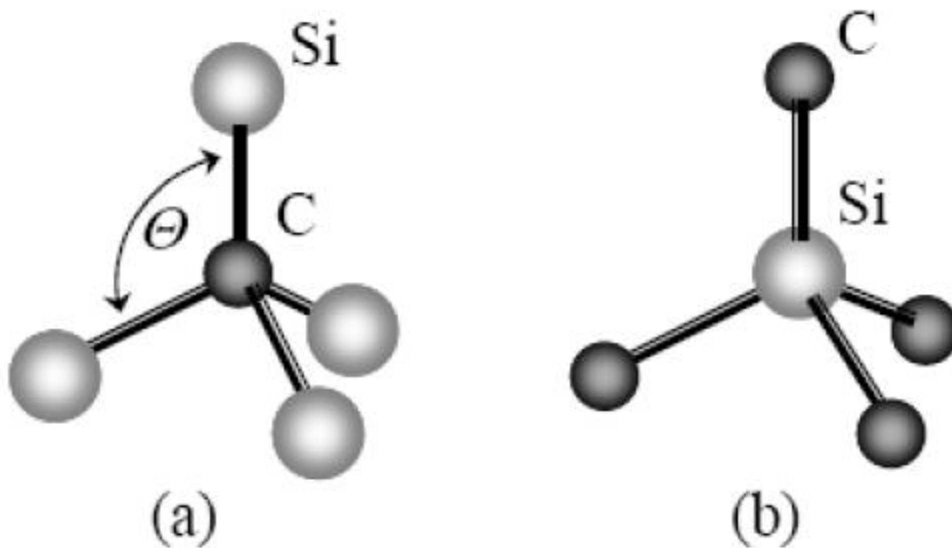

Figure 1.5: *Tetrahedron showing (a) one carbon bonded to 4 silicon atoms and (b) one silicon bonded to 4 carbon atoms. Taken from [18].*

SiC is a group IV-IV stable compound semiconductor that exists in multiple structural polytypes which depends on the stacking order of the Si-C bilayer [7]. The polytypes can be well-described as the ability of a crystal to crystallize in many different crystal structures. Out of more than 250

SiC polytypes, the most common are 3C-SiC (β-SiC), 2H-SiC, 4H-SiC, 6H-SiC and 15R-SiC. The numbers represent the repetition of the Si-C bilayers whereas C, H, and R represent cubic, hexagonal, and rhombohedral crystalline Bravais lattice varieties [7]. 3C-SiC is the only one with a cubic crystal structure. Atoms in 3C-SiC prearrangement are closely packed. Ramsdell notation is utilized to depict in detail the polytypes of SiC. The Ramsdell's notation is applicable to distinguish all closed-packed structures. The 2H-SiC unit cell is composed of A and B layers stacked as ABAB… the symmetry is hexagonal (Wurtzite) while the 4H-SiC is two times longer than the 2H-SiC, its stacking sequence is ABCBABCB…it consists of an equal number of cubic and hexagonal bonds. The 6H-SiC is three times longer than the 2H-SiC and its stacking sequence is ABCACBABCACB… [21]. 3C-SiC has the stacking sequence of ABCABC…. of the face centered Bravaais lattice. This crystallographic structure is known as cubic (zinc-blende) [30]. The 15R-SiC is made both the cubic and the hexagonal bonds [7]. Its stacking sequence is given as ABCACBCABACABCB… These types are demonstrated in Figure 1.3.

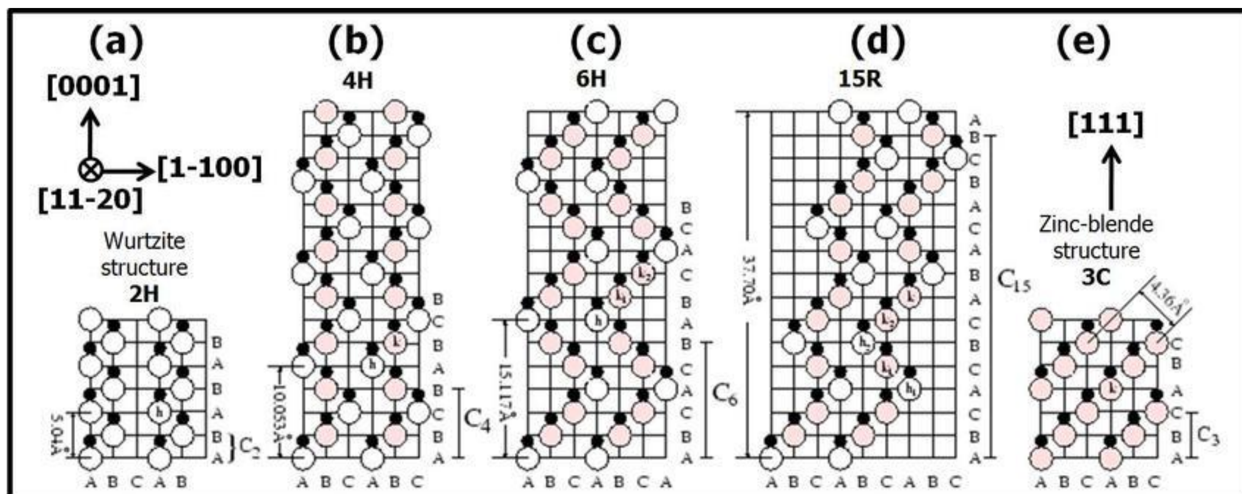

Figure 1.6: *The stacking sequence for SiC polytypes in the 1120 plane. (a) 2H-, (b) 4H-, (c) 6H-, (d) 15R- and (e) 3C-SiC. Taken from [8].*

1.3 Previous studies of Ag and Sr migration behavior in SiC

In order to attain a reduction of fission product releases from TRISO particles, it is vital to study the fundamental mechanism by which the FPs migrate through SiC. Extensive work related to migration behavior of Ag in SiC has been reported [9,12,14,19,23-31] while limited work has been detailed on the migration behavior of Sr in SiC [28,32,33].

A study by Friedland *et al.* [14] investigated silver (Ag) diffusion in polycrystalline and single 6H-SiC. In their study, Ag of 360 keV was implanted at room temperature (RT), 350 ℃, and 600 ℃. With samples implanted at 350 ℃ they observed a strong diffusion of Ag after isothermal annealing at 1300 ℃ for 10 hours in both polycrystalline and single crystalline SiC. This diffusion was attributed to implantation induced radiation damage. No additional diffusion took place in the 6H–SiC samples when they further annealed at this temperature for 80 hours, while in the polycrystalline-SiC diffusion was considerably reduced. They described that the diffusion reduction in polycrystalline-SiC could be due to grain boundary obeying Fickian diffusion. They further performed isochronal annealing of polycrystalline SiC up to 1400 ℃. They concluded that Ag diffuses along the boundary grains at temperatures above 1100 ℃ in polycrystalline SiC [14]. Another study by Hlatshwayo *et al.* [9] on the annealing of silver implanted into 6H-SiC showed that Ag implanted at room temperature created amorphous layers from the surface while samples implanted at 350 ℃ and 600 ℃ retained the crystal structure. They further observed that annealing the room temperature (RT), implanted samples at 1300 ℃ for 10 hours caused broadening of the Ag profile. The authors concluded that Ag started to diffuse at 1300℃.

Malherbe *et al.* [24] studied the SEM analysis of 360 keV Ag ions implanted at room temperature (RT) and at 600 ℃ were vacuum annealed from 900℃ to 1600℃. They observed that with modern scanning electron microscopy coupled with in-lens detector systems, it is possible to detect crystal defects. At room temperature (RT) they observed voids spread out in the implanted layer whereas at high temperature implanted 6H-SiC was observed to retain crystallinity [24]. A study by Shrader *et al.* [23] on Ag diffusion in cubic SiC showed Ag to diffuse towards the bulk of SiC. The diffusion of Ag impurities in bulk of 3C-SiC was studied using *ab initio* methods that are based on density functional theory. The authors reported that Ag defects consist of Ag_c, Ag_{si},

substitutions, Ag interstitials, and Ag-vacancy defect complexes. In their study, Ag was identified in defect cluster and found on the silicon sub-lattice site [23].

Friedland *et al.* [32] also investigated the influence of radiation damage on strontium and iodine diffusion in silicon carbide [32]. Sr diffusion in SiC was observed after hot implantations and the diffusion of Sr was dominant during initial stages of post implantation annealing. They also reported grain boundary and volume diffusion of Sr was observed at high temperature. Sr during isothermal annealing could not be detected due to the grain boundary and volume diffusion. Friedland *et al.* [33] observed trapping of implanted Sr into the bulk but released by defects at different temperatures [33]. Another study on Sr diffusion is reported by Abdelbagi *et al.* [28]. Their work was based on samples that were implanted with 360 keV Sr ions at room temperature and irradiated with 167 MeV Xe ions to a fluence of $3.4 \times 10^{14}\ cm^{-2}$ and $8.3 \times 10^{14}\ cm^{-2}$. The migration of Sr was observed in both irradiated and un-irradiated samples. The samples implanted with Sr and un-irradiated retained Sr at 1500 °C while the irradiated samples in both fluences no Sr was retained after annealing at 1300 °C and 1400 °C. Also the authors observed decomposition of SiC in all samples after annealing at 1500 °C [28].

1.4 Motivation of this study

Fission products co-exist in a nuclear reactor hence their synergetic effects need to be investigated, giving understanding in the migration behavior in SiC. The migration behavior of Ag and Sr have been investigated without taking into account the effect of the other FPs. However, few researchers have investigated the synergistic effects of either Ag or Sr with other FPs. Few studies have been reported on palladium (Pd) and Ag [18], iodine (I) and Ag [18,35] and Ruthium (Ru) and Ag [36] into SiC (which has not been thoroughly investigated).

A study by Lauf [34] on the interaction of silver and palladium with silicon carbide in fuel particles [18] showed that Ag and Pd attack the SiC layer of fuel particles. The Pd attack on the SiC increases as the annealing temperature was increased. As samples were annealed, Ag appeared to migrate more rapidly than the attack of Pd on SiC [34].

Hlatshwayo *et al.* [35] co-implanted iodine and Ag ions into 6H-SiC at room temperature (RT) [35]. 360 keV of both I and Ag ions were single and co-implanted into 6H-SiC at room temperature

(RT). Co-implantation of the ions caused amorphization of the 6H-SiC matrix from the surface. Annealing the amorphous 6H-SiC at 1500 ℃ for 30 hours caused epitaxial growth from the bulk damaged interface. Iodine assisted Ag in its retainment in 6H-SiC at high annealing temperatures [35]. Kuhudzai *et al.* [18] also investigated the synergistic effect of iodine and silver ions co-implanted in 6H-SiC [18]. Annealing the sample at 1500 ℃ for 30 hours demonstrated that the presence of iodine has a synergetic effect in retaining Ag in SiC. Iodine role was observed by the authors to enhance the recrystallization of SiC during annealing which played an essential role in the immobilization of Ag. The authors used the atom probe tomography (APT) which enabled them to observe a clear spatial association clusters of Ag and I. The authors concluded that the retention of Ag is due to I. O'Connell *et al.* [36] investigated the role of Ru and Ag implanted in the SiC. The researchers observed that Ru aided the migration of Ag in SiC [36].

In this study, the effects of Ag and Sr ions co-implanted into polycrystalline silicon carbide were studied. The outcome of the current study is vital in understanding the migration behavior of these FPs in an environment that closely resembles nuclear reactor environments. Ag and Sr ions were co-implanted into polycrystalline SiC at 600 ℃. The co-implanted samples were then annealed from temperatures rage 1000 ℃ to 1400 ℃ in steps of 100 ℃ for 5 hours. The structural evolution and surface morphology were monitored by Raman spectroscopy and scanning electron microscopy (SEM). Rutherford backscattering spectrometry (RBS) was used to monitor the migration behavior of implanted species.

1.5 Outlay of the Dissertation

The remaining chapters of this dissertation is structured as: Chapter 2 gives description on diffusion theory. In chapter 3, discussion of ion implantation. The characterization methods are discussed in chapter 4. Sample preparation is described in chapter 5. Chapter 6 presents and discusses the results. Chapter 7 gives conclusions and future studies.

References

1. Special Report of the intergovernmental panel on climate change (IPCC). Renewable energy sources and climate change mitigation. *Summary for policymakers and technical Summary. Cambridge University Press*. ISBN 978-92-9169-131-9. 2012. Available online at www.ipcc.ch [Accessed on 12th July, 2019].
2. F. Alam, R. Sarkar, H. Chowdhury. Nuclear power plants in emerging economies and resource development: A review. *Energy Procedia*. 160(2019)3-10.
3. World Nuclear Association, Electricity generation- what are the options?. Available online at: https://www.world-nuclear.org/nuclear-basics/electricity-generation-what-are-the-options.aspx [Accessed on 10th July, 2019].
4. M. Ho, E. Obbard, P.A. Burr, G. Yeoh. A review on the development of nuclear power reactors. *Energy Procedia.* 160 (2019)459-466.
5. R.J. Kuhudzai, Diffusion and surface effects for SiC implanted with fission product elements. *Ph.D. thesis. University of Pretoria*. 2015.
6. G. Donald, The pebble bed modular reactor. *Spring 2002: EEE460WebProject* (2002)
7. J.B. Malherbe, Diffusion of fission products and radiation damage in SiC. *Journal of Physics. D: Applied Phys*ics 46 (2013)47-3001
8. T.T. Thabethe. The interfacial reaction and analysis of W thin film on 6H-SiC annealed in vacuum, hydrogen and argon. *Ph.D. thesis. University of Pretoria* 2017
9. T.T. Hlatshwayo, J.B. Malherbe, N.G. van der Berg, L.C. Prinsloo, A.J. Botha, E. Wendler, W. Wesch. Annealing of silver implanted 6H-SiC and diffusion of the silver. *Nuclear Instruments and Method in Physics Research B* 274(2012) 120-125.
10. R.J. Kuhudzai, Diffusion of ion implanted iodine in 6H-SiC. *Master's dissertation. University of Pretoria.* 2010
11. T.M. Mohlala, T.T. Hlatshwayo, M. Mlambo, E.G. Njoroge, S.V. Motloung, J.B. Malherbe. Migration behaviour of europium implanted into single crystalline 6H-SiC. *Vacuum* 141 (2017) 130-134
12. T.T. Hlatshwayo. Diffusion of Silver in 6H-SiC. *PhD thesis. University of Pretoria.* 2010

13. IAEA. High Temperature Gas-Cooled Reactor Fuels and Materials. *International Atomic Energy Agency*, Vienna. 2010. IAEA-TECDOC-1645. ISBN 978-92-0-1531-10-2, ISSN 1684-2073
14. E. Friedland, J.B. Malherbe, N.G. van der Berg, T. Hlatshwayo, A.J. Botha, E. Wendler, W. Wesch. Study of Silver diffusion in silicon carbide. *Journal of Nuclear Materials* 389 (2009) 326-331
15. U.S. DEPARTMENT OF HEALTH AND HUMAN SERVICES Public Health Service Agency for Toxic Substances and Disease Registry. Toxicological profile for strontium. 2004. Available online at: https://www.atsdr.cdc.gov/toxprofiles/tp159.pdf [Accessed on 14th July, 2019]
16. W. Zhou, Y. Zhang, G. Min. One-Dimensional SiC Nanostructures: Synthesis and Properties. *RsearchGate,* 2008. DOI: 10.1007/1978-0-387-74132-1_2
17. P. Kwasnicki. Evaluation of doping in 4H-SiC by optical spectroscopies. Materials science [condmat.mtrl-sci]. Universite Montpellier II- Sciences et Techniques du Launguedoc.2014
18. R.J. Kuhudzai, J.B. Malherbe, T.T. Hlatshwayo, N.G. van der Berg, A. Devaraj Z. Zhu, M. Nandasiri. Synergistic effects of iodine and silver ions co-implanted in 6H-SiC. *Journal of Nuclear Materials*. Volume 467, Part 2, (2015), pp. 582-587
19. N.G. van der Berg, J.B. Malherbe, A.J. Botha, E. Friedland, Thermal etching of SiC. Applied Surface Science 258 (2012) 5561-5566
20. A.A. Suvorova, S. Samarin, Secondary electron imaging of SiC-based structures in secondary electron microscope. *Surface Science,* 610 (18), 2007, p.4428-4432
21. Wikipedia. Polymorphs of silicon carbide. Accessed on 29 October 2019. Available from: https://en.wikipedia.org/wiki/Polymorphs_of_silicon_carbide#Summary_of_polytypes
22. Openstax. Chemistry-liquids and solids. Accessed on: 22 October 2019. Available from: https://opentextbc.ca/chemistry/chapter/10-6-lattice-structures-in-crystalline-solids/
23. D. Shrader, S.M. Khalil, T. Gerczak, T.R. Allen, A.J. Heim, I. Szlufarska, D. Morgan. Ag diffusion in cubic silicon carbide. *Journal of Nuclear Materials*. 408(2011) 257-271
24. J.B. Malherbe, N.G. van der Berg, A.J.Botha, E. Friedland, T.T Hlatshwayo, R.J. Kuhudzai, E. Wedler, W. Wesch, P. Charkraborty, E.F. da Silveira. SEM analysis of ion implanted SiC. *Nuclear Instruments and Methods in research B*, 315 (2013)136-141

25. H. Nabielek, P.E. Brown, P. Ofermann, Silver release from coated particle fuel. *Nuclear Technology*, 35(1977) 483-93
26. T.T. Hlatshwayo, J.B. Malherbe, N.G. van der Berg, A.J. Botha, P. Chakraborty, Effect of thermal annealing and neutron irradiation in 6H-SiC implanted with silver at 350 C and 600C, *Nuclear Instruments and Methods Physics Research B* 273(2012) 61-64
27. E. Friedland, N. G. van der Berg, J. B. Malherbe, J. J. Hancke, J. R. N. Barry, E. Wendler and W. Wesch, Investigation of silver and iodine transport through silicon carbide layers prepared for nuclear fuel element cladding. *Journal of Nuclear Material* 410 (2011) 24 - 31.
28. H. A. A. Abdelbagi, V. A. Skuratov, S. V. Motloung, E. G. Njoroge, M. Mlambo, J. B. Malherbe, J. H. O'Connell and T. T. Hlatshwayo, Effect of swift heavy ions irradiation in the migration of silver implanted into polycrystalline SiC. *Nuclear Instrument Methods Physics Research B* 461 (2019) 201-209.
29. H. J. MacLean, R. G. Ballinger, Silver ion implantation and annealing in CVD silicon carbide: the effect of temperature on silver migration. Second Topical Meeting on High Temperature Reactors 2004 (HTR-2004), Beijing, China, (2004) 22 - 24.
30. J. J. van der Merwe, Evaluation of silver transport through SiC during the German HTR fuel program. *Journal of Nuclear Material* 395 (2009) 99-111.
31. H. Nabielek, P. E. Brown and P. Offermann, Silver release from coated particle fuel. *Nuclear Technology* 35 (1977) 483 - 493.
32. E. Friedland, N.G. van der Berg, J.B. Malherbe, E. Wendler, W. Wesch. Influence of radiation damage on strontium and iodine diffusion in silicon carbide. *Journal of Nuclear Materials* 425(2012) 205-210
33. E. Friedland, T. Hlatshwayo, N.G. van der Berg, Influence of radiation damage on diffusion of fission products in silicon carbide. *Physica Status Solidi C* 10(2013) 208-215
34. R.J. Lauf. Interaction of Silver and palladium with silicon carbide in HTGR fuel particles. *Preliminary report*. (1980). Available from: DOI:10.2172/5137293
35. T.T. Hlatshwayo, N.G. van der Berg, M. Msimanga, J.B. Malherbe, R.J. Kuhudzai, Iodine assistance retainment of implanted silver in 6H-SiC at high temperatures, *Nuclear Instruments and Methods in Physics Research B* 334(2014)101-105

36. J. O'Connell, J. Neethling, Palladium and ruthenium supported silver migration in 3C-silicon carbide, *Journal of Nuclear Materials*, 456(2015)436-441

Chapter 2: Diffusion

Diffusion is the movement of atoms from a region of high concentration to a region of low concentration [1]. In solid materials, atoms are continually vibrating approximately to their lattice site. For an atom to move about its lattice site it must have adequate energy to break the bonds with its neighbouring atoms [1]. The random movement of atoms results in a flux of atoms from regions of high concentration towards the regions of low concentration. This net flux of atoms depends on the concentration gradient.

2.1 Diffusion mathematics

It is important to recognize how quickly the atoms move from a region of high concentration to a region of low concentration. Fick's first law states that the net flux of atoms is directly proportional to the concentration gradient [2]:

$$J = -D\frac{dC}{dx} \tag{2.1}$$

where, J is the mass flux; mass flow from high concentration to low concentration, D is the diffusivity or known as the diffusion coefficient. Diffusivity depends on diffusion mechanism, temperature of diffusion, type of crystal structure, concentration of diffusion species and crystal imperfections. $\frac{dC}{dx}$ is the diffusion gradient and C is the concentration of the diffusing substance [2]. The negative sign in Equation (2.1) indicates that the flux direction is from high concentration to low concentration while the concentration gradient is from low concentration to high concentration. The concentration gradient changes with time in the steady state diffusion and is described by Fick's second law. Fick's second law states that the rate of compositional change is equal to diffusivity times the rate of change of the concentration gradient [2]. Considering the continuity equation in Equation (2.1) and the diffusion to be in the positive x direction then:

$$\frac{\partial C}{\partial t} = \frac{\partial}{\partial}\left(D\frac{\partial C}{\partial x}\right) = D\frac{\partial^2 C}{\partial x^2} \tag{2.2}$$

In 3 dimension, Equation (2.2) is written as:

$$\frac{dC}{dt} = D\nabla^2 C \tag{2.3}$$

In a limited temperature range, the temperature dependence of the diffusivity is given by Arrhenius equation [2.4]:

$$D = D_o e^{\left(-\frac{E_a}{k_B T}\right)} \tag{2.4}$$

where, D_o is the proportionality constant that is independent of temperature, and E_a is the activation energy, T is the absolute temperature in units of Kelvin and k_B is Boltzmann's constant.

2.2 Mechanism of diffusion in solids

Diffusion mechanism in solids helps in understanding the physical changes and behaviour of the material. This section discusses the main diffusion mechanisms in solids.

2.2.1 Vacancy mechanism

All crystals have unoccupied lattice positions called vacancies. These vacancies are created when the solids are formed. They occur naturally because of thermal vibrations. Self-atoms can move from one site to another if there is enough energy for the atom to overcome activation energy and if there are vacancies present for the atom to move into [3]. An example of a vacancy mechanism is shown in Figure 2.1 (a) and (b) where in this case we have B (grey) atoms with similar size as A (black) atoms. The B (grey) atoms can migrate to the nearest vacant site.

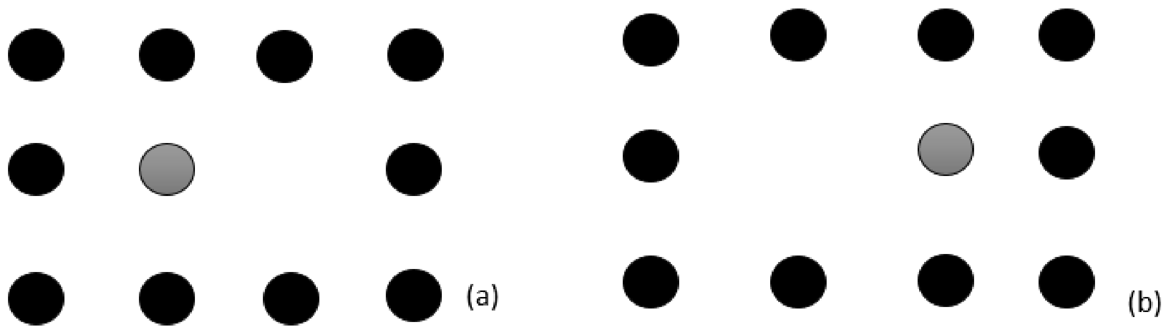

Figure 2.1: *Schematic representation of the vacancy diffusion mechanism. The empty space represents the vacancy and the grey and black circles represents atoms. (a) and (b) shows the positions before and after diffusion respectively.*

2.1.2 Interstitial mechanism

Interstitial diffusion is a diffusion mechanism in which impurity atoms move between the host atoms and occupy space outside the normal lattice position. In Figure 2.2, the interstitial atom (the small B (grey) atoms) are relatively smaller than the A (black) atoms. B (grey) atom moves from one interstitial position to another interstitial position in all possible neighbouring positions making use of the gap between the host atoms. However, the interstitial atom cannot make a direct move to jump the A atoms (black) [4].

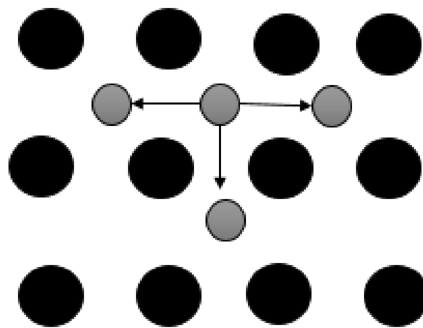

Figure 2.2: *Interstitial mechanism (a) before and (b) after an interstitial diffusion*

2.1.3 Dislocation and Grain boundary

Dislocation and grain boundary are one and two dimensional defects respectively. Both these defects are fast diffusion paths. Grain boundaries are found in polycrystalline solids; they are the interface between two crystallites. They can act as sinks and a transport pathway for point defects. Dislocations are usually extra incomplete planes within the lattice structure. Examples of dislocation are screw, mixed and edge dislocations. Dislocations occur when stress is applied to the matrix i.e when annealed at high temperatures.

2.3 Diffusion in polycrystalline SiC

A crystalline solid is a solid material whose ions, molecules or atoms are arranged in definite repeating patterns in three dimensions forming a crystal. Polycrystalline SiC solid is composed of many single crystalline 6H-SiC regions that vary with size, shape and orientation. The crystalline

regions are called grains and the separations between the grains are called grain boundaries [5]. The material compositions in polycrystalline SiC make diffusion more complex. Diffusion species can migrate via grain boundary and certain crystalline defects such as dislocations [6].

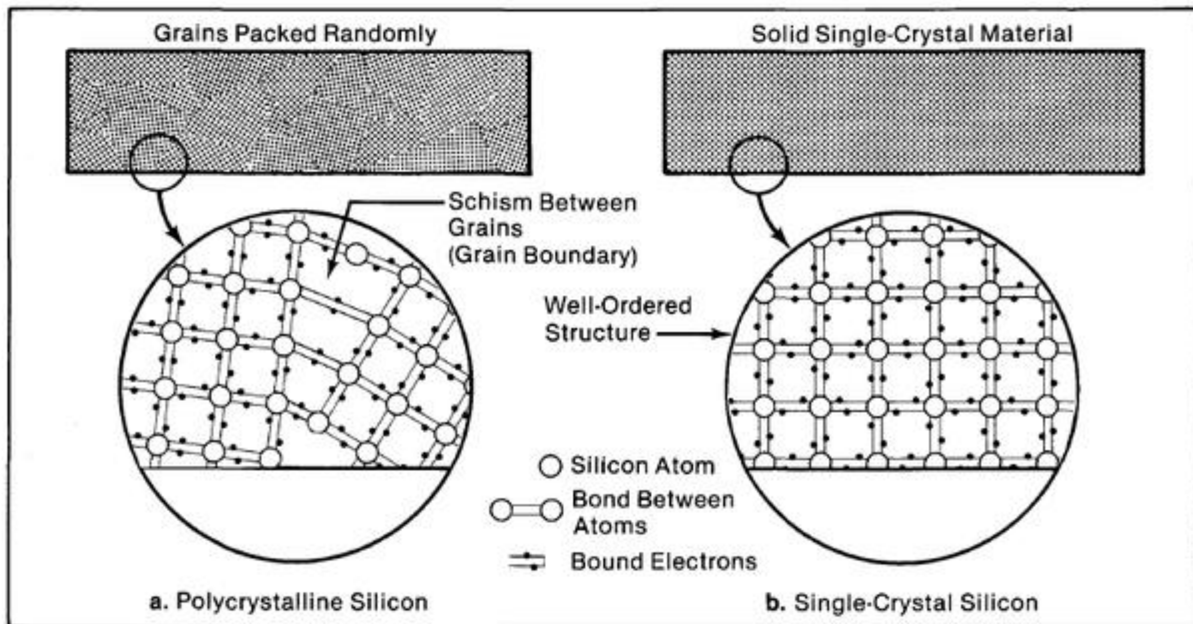

Figure 2.3: *Illustration of (a) polycrystalline and (b) single crystalline. Taken from [9].*

2.4 Evaluation of the diffusion coefficient

There are many ways of evaluating the solution of the diffusion Equation (2.2). Crank [7] discusses in the book entitled "*The Mathematics of Diffusion*" the variation of boundary conditions [7]. They all require the measurement of the implanted species profile. In this work, no diffusion coefficient of implanted species was evaluated. This was due to the fact that Rutherford backscattered spectroscopy (RBS) could not separate Ag and Sr co-implanted into SiC. This will be discussed in chapter 6.

References

1. D. Shaw. Atomic Diffusion in Semiconductor. *Plenum Press, London* (1973). P.3
2. A. Fick, Ueber Diffusion. *Annalen der Physik*. Leipzig. 170 (1855) 59.
3. P. Shewmon, Diffusion in solid. The Minerals, Metals and Materials Soc., USA. (1989)
4. W. D. Callister, D. G. Rethwisch, Materials science and engineering an introduction. 7th edition, John Wiley, USA. (2007) 122.
5. J. M. Poate, K. N. Tu and J. W. Mayer, Thin films-inter diffusion and reactions. John Wiley, USA. (1978) 578.
6. T.M. Mohlala. Migration behavior of Europium implanted into single crystalline 6H-SiC. MSc dissertation. *University of Pretoria.* 2017
7. J. Crank. The Mathematics of Diffusion, *Oxford University Press, Bristol* (1975). P.2

Chapter 3: Ion implantation

Ion implantation is a process in which ions are accelerated into a material thereby changing the physical, chemical or electrical properties of the material. The ions directed towards the material collide with the host atoms thus losing their energy and eventually halt at a certain depth within the target [1]. The ions lose their energy via elastic and inelastic collisions within the material. This process is utilized in semiconductor device fabrication and in material finishing, as well as in material science research. When using this technique, the prediction of the ultimate dispersal of ions within the material is vital. This is accomplished when all the processes included are understood and ions inside the target material come to rest. Subsequently, this chapter depicts the vital processes that happen amid ion implantation.

3.1 Stopping power

The energy loss within the material is the element that affects the final distribution of ions and defects. Tesmer *et al.* [2] define the stopping power (S) as the average energy loss (E) per unit path length (x) of the particle due to the interactions with the target atoms [2]:

$$S = \frac{dE}{dx} \tag{3.1}$$

x in Equation (3.1) is the length from the surface of the target to where the ion come to rest within the target.

When energetic ions penetrate a material they lose their energy via two major processes that are independent of each other called the electronic stopping and the nuclear stopping. The nuclear stopping is due by elastic collisions between the projectile ion and target atom in the host material. The electronic stopping is caused by inelastic collisions between the ion and electrons of target atom. These two aspects are discussed in sections 3.1.1 and 3.1.2 respectively. The sum of these two energy loses can be mathematically defined as [3]:

$$S = \left(\frac{dE}{dx}\right)_n + \left(\frac{dE}{dx}\right)_e \tag{3.2}$$

The subscripts n and e represent nuclear and electronic stopping respectively.

From Equation (3.1), the stopping cross-section can be determined by division of total stopping power S and density N:

$$\frac{S}{N} = \varepsilon = -\frac{1}{\mathrm{N}}\left(\frac{\mathrm{dE}}{\mathrm{dx}}\right)$$

where, ε is the stopping cross-section.

Equation (3.2) can be written as:

$$\varepsilon = \left[-\frac{1}{\mathrm{N}}\left(\frac{\mathrm{dE}}{\mathrm{dx}}\right)_{\mathrm{n}}\right] + \left[-\frac{1}{\mathrm{N}}\left(\frac{\mathrm{dE}}{\mathrm{dx}}\right)_{\mathrm{e}}\right]$$

Thus, $\varepsilon = \varepsilon_{\mathrm{n}} + \varepsilon_{\mathrm{e}}$

where, ε_{n} and ε_{e} are the nuclear and electronic stopping cross-section.

The penetration length R of the incident ions with incident energy $E_o$is given by integrating the energy loss [3]:

$$R = \int_0^{E_o} \frac{dE}{S} = \frac{1}{N}\int_0^{E_o} \frac{dE}{dE/dx} \tag{3.3}$$

Figure 3.1 shows the nuclear and electronic stopping as a function of ion incident energy (E).

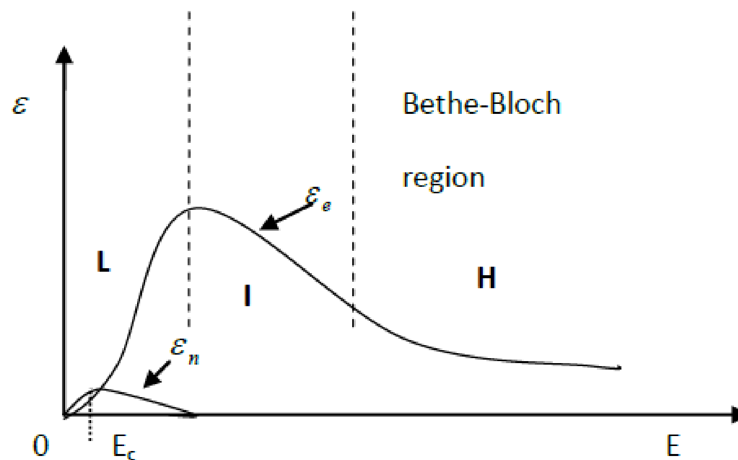

Figure 3.1: *The nuclear, ε_n, and electronic, ε_e, stopping power as a function of ion energy, E. Taken from [4].*

In Figure 3.1 there are three energy regions: L, the low energy region where $V_1 < V_o Z^{\frac{2}{3}}$, the intermediate region, I, where $V_1 \approx V_o Z^{\frac{2}{3}}$, and the high energy region, H, where $V_1 \gg V_o Z^{\frac{2}{3}}$. V_1 and V_o are the velocities of the ion and the Bohr velocity respectively while Z is the atomic number of the ion. The nuclear stopping is dominant at low energies whereas the electronic stopping is dominant at high energies. Above critical energy, E_c, electronic stopping starts to dominate after reaching a maximum and then losses energy in the high region. At the high energy region, the ion has a very short period to collide with the targeted atoms due to its high velocities. The low and intermediate energy loss is detailed in subdivisions below.

3.1.1 Nuclear stopping

Nuclear stopping is a phenomenon whereby charged particles lose their energy via elastic collision with the target atom. The charged particle is strongly deflected and lattice atoms are knocked out. When an implanted ions interact with the target atom the cations are repelled by the positive cores of the target ions through Coulomb potential. The Coulomb potential between two nuclei is given by [5]:

$$V_c(r) = \frac{e^2 Z_1 Z_2}{4\pi\varepsilon_o r} \tag{3.4}$$

where Z_1 and Z_2 are the atomic number of the implanted ion and of the target particle, respectively, ε_o is the permittivity of free space, r is the distance between nuclei and e is the electronic charge. Since these particles are close to each other the Coulombs potential becomes [5]:

$$V(r) = V_c(r)\emptyset\left(\frac{r}{a}\right) \tag{3.5}$$

where, $\emptyset$ is the screening function for the Coulomb potential, a, is the screening length and $\frac{r}{a}$, is called the reduced radius. Both the screening potential and screening distance are used to model elastic collision processes to testify the requirement for both small and large impact parameters.

A theoretical description of the collision is illustrated below in Figure 3.2 which depicts that the implanted ion with mass M_1 (black) at velocity V_1 collides with a stationary mass M_2. The collision between the masses is elastic. This means both kinetic energy and momentum are conserved.

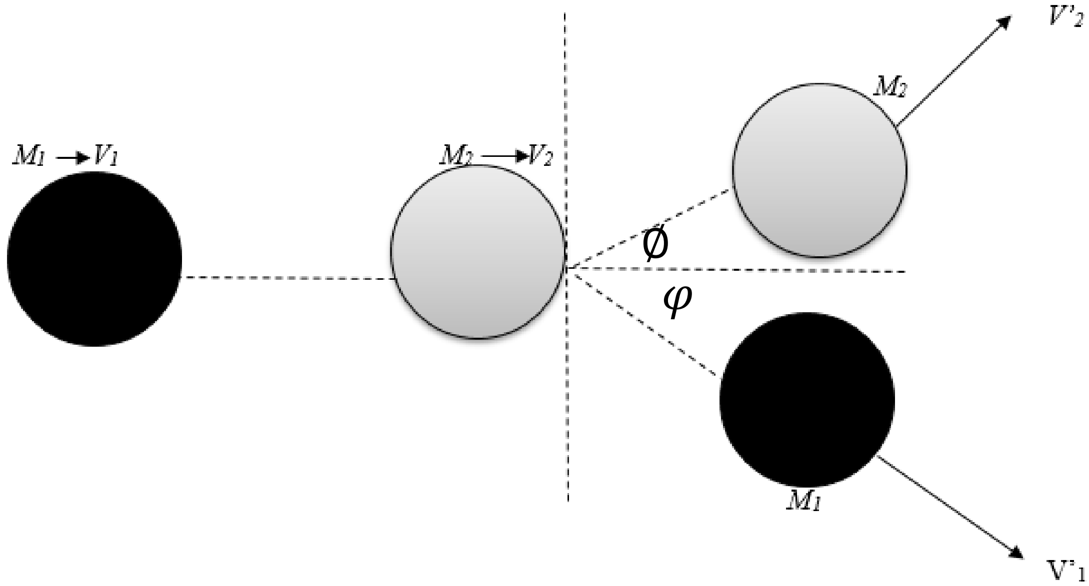

Figure 3.2: *A typical nuclear elastic collision between the initial momentum of M_1 and stationary target atom of M_2 and the final momentum of the M_1 and M_2.*

Considering the problem from the centre of mass frame we obtain [2,5]:

$$T = \frac{4M_1M_2}{(M_1+M_2)^2} E_o sin^2\left(\frac{\theta}{2}\right) = T_{max} sin^2\frac{\theta}{2} \tag{3.6}$$

T is the transferred energy, θ, is the scattered angle. The energy, T, is lost by the projectile to the atom and it depends on the scattered angle. The maximum transferred energy, T_{max}, occurs in a head-on collision $(\theta = \pi)$ and when the projectile and the atom are of equal mass. The rate of the energy loss due to collision per unit path length is the sum of energy loss multiplied by the probability of an occurrence of the collision [3]:

$$\mathcal{E}_n = \left(\frac{dE}{dx}\right)_{nuclear} = N \int_0^{T_{max}} T d\sigma \tag{3.7}$$

$\mathcal{E}_n$ is the nuclear energy loss, N is the number of target atom per unit volume and $d\sigma$ is the differential cross section. Due to the conservation of energy of the collision, the transferred energy causes the stationary atom recoils at an angle, θ and this damages the lattice site [2].

3.1.2 Electronic stopping

Electronic stopping is whereby an excited ion impinge the material and lose energy via inelastic collisions with targeted electrons. The energy transferred from the ion to the target electrons is a complex process because it arises from complex methods. A few of these processes have been researched and studied by Ziegler *et al.* [7]. The energy loss process is usually partitioned into three parts based on the ion velocity with the Bohr velocity as shown in Equation (3.8):

$$v_o = \frac{e^2}{\hbar} \quad (3.8)$$

where, v_o is the Bohr's velocity, e is the electron charge and $\hbar$ is the Plank's constant. In Figure 3.1 the L region deals with the ion's velocity $V_1 < V_o Z^{2/3}$. The $V_o Z^{2/3}$ for silver and strontium ions is $2.8 \times 10^9\ {cm}/_{s}$ and $2.5 \times 10^9\ {cm}/_{s}$ respectively. At $360\ keV$ ion energy silver and strontium have an initial velocity of $8 \times 10^7\ {cm}/_{s}$ and $8.9 \times 10^7\ {cm}/_{s}$ respectively, which is less than actual value of $V_o Z^{2/3}$. In the L region, no sufficient energy can be transferred to the electrons that are lower in energy than the Fermi level to energize to vacancy. In calculating the electronic stopping for the L region, a thickness ρ is assumed for a free electron gas [8]. Thus, the electronic stopping cross section can be written as [9]:

$$\varepsilon_e = \int I(v, \rho)\big(Z(v)\big)^2 \rho dV \quad (3.9)$$

where ε_e is the electronic stopping, I is the interaction stopping function of the ion of a unit charge with velocity v. Z_1 is the atomic number of the incident ion, and ρ is the electron density of each volume element of the target dV.

In the H region in Figure 3.1 is described by the Bethe-Bloch equation for high velocities that is given by the condition $V_1 >> V_o Z^{2/3}$. The electronic stopping in this region is proportional to ${Z_1}^2$ as given in Bethe-Bloch equation [10]:

$$\varepsilon_e = \frac{4\pi {Z_1}^2 {Z_2}^2 e^4}{m_e {V_1}^2}\left[ln\left(\frac{2m_e {V_1}^2}{I}\right) + ln\left(\frac{1}{1-\beta^2}\right) - \beta^2 - \frac{C}{Z_2} - \frac{\delta}{2}\right] \quad (3.10)$$

where m_e is the mass of electron, V_1 the velocity of the projectile, β is the velocity of the projectile divided by the speed of light ($\beta = {}^{v}/_{c}$). $\frac{C}{Z_2}$ is the shell correction, δ is the density function at very high kinetic energies, and I is the mean excitation potential which is defined theoretically as [11]:

$$lnI = \sum_n f_n ln(E_n - E_o) \tag{3.11}$$

where $f_n$is the corresponding oscillator strengths for target atoms, $E_o$and $E_n$are the ground state and the possible energy transitions respectively. An estimate for I is given by Block's rule [12]:

$$I = (10\ eV)Z_2 \tag{3.12}$$

The third part is the intermediate region, that is between part 1 and part 2; the region where $V_1 \approx V_o Z^{2/3}$.

For the work presented in this dissertation, the important domains are in the low and intermediate energy loss regions as depicted in Figure 3.1. The low energy region is for the implantation of silver and strontium of 360 keV into SiC and intermediate energy regime for the Rutherford backscattering spectrometry (RBS) where using 1.6 MeV α- particles are used to measure the implanted ions in the SiC. The $V_o Z^{\frac{2}{3}}$ for α- particle is $3.5 \times 10^9\ {}^{cm}/_{s}$. At 1.6 MeV ion energy, α- particle has an initial velocity of $8.77 \times 10^9\ {}^{cm}/_{s}$, which is close to the value of $V_o Z^{\frac{2}{3}}$.

3.2 Energy loss in compounds

Thus far a target comprising of a single element has been discussed. The energy loss in targets comprising of multiple elements is presented in this work, that is SiC. This section discusses the energy loss in compounds.

The total stopping of an ion penetrating a compound $A_x B_y$ consisting two different elements A and B can be determined by additive rule. This rule is known as the Bragg rule [13] where the stopping cross section of element A and B are written as ε^A and ε^Brespectively. This is shown in Equation (3.13):

$$\varepsilon^{A_x+B_y} = x\varepsilon^A + y\varepsilon^B \tag{3.13}$$

where x and y are the relative molar fractions of the compound consisting of elements A and B.

Experimentally, the energy loss from the Bragg's rule have been found to deviate slightly via the chemical state and physical state of the target. Deviations of the array 10% to 20% from the Bragg rule have been observed for the stopping maximum for solid compounds. The deviations are particularly apparent when large contrasts amid the atomic masses of the constituents such as in the case of oxides [9]. These deviations led to the improvement of the Core and Bonds model (CAB) with regard to improving the chemical state of the compound [9]. In compounds it is assumed that the stopping of ions is via two contributions: The impacts of the non-bonding core and the bonding valence electrons. To determine CAB improvement, the bond structure must be known.

3.3 Energy straggling

Straggling occurs when an excited ion moving through a material loses its energy by means of numerous interactions with the target's atoms, which lead to factual variances. This infer that identical energetic ions with the same initial energy when penetrating the target will not have equal energies after passing the same thickness x of the same target [3]. In the electronic energy loss, the straggling is derived from the Bloch-Bethe equation discussed in Equation (3.10). This Bohr straggling is given by:

$$\Omega_B{}^2 = 4\pi Z_1{}^2 Z_2{}^2 e^4 N x \tag{3.14}$$

where $\Omega_B{}^2$is the energy loss of a projectile after passing a target thickness x. The distribution of the energy loss which arises from various independent collisions becomes roughly Gaussian when the energy loss is small compared to the incident energy [13]. In a compound target, the total energy straggling is established by a linear additivity rule in a similar way to the Bragg's rule for energy loss [2].

3.4 Range and Range straggling

There are different parameters used to quantify the distance that an energetic ion travels in a solid. These include, range (R), projected range (R_p), penetration depth (X_s), and projected range straggling (ΔR_p). The easiest way to define these parameters is to establish the interaction of a single ion with a solid material. The implantation behaviour of a single ion can be generalized to

reflect the implantation behaviour of several ions [15]. Initially the ions in ion beam have the same energy. When the energetic ion is accelerated inside the solid, the interaction between the primary ion and the target occur via Coulombic interaction. As a result, if the ion does not backscatter out of the target surface, the ion lose energy until it's (almost) zero. Therefore, according to the range of theory the distance travelled by the ion from the ion beam to the resting position is called the range (R). The range (R) gives the proximity depth which the ion reaches in the target before coming to rest.

The range (R) can be calculated using the Equation (3.3) given in section 3.1. The range (R) can be defined as integrated distance that an ion travels while moving in a material which inversely acknowledges the stopping power [16]. The ion lose energy over the interval $0 \leq E \leq E_o$, where E_o is the energy of the incident ion beam.

When ions have high energy, their path is straight because the electronic stopping dominates over the nuclear stopping. As the velocity decreases and the energy of the ion is low, the path length is a zigzag because nuclear stopping dominates at low energies over the electronic stopping. A diagram illustrating the path length travelled by a single ion is shown in Figure 3.3. This illustration discloses that the range (R) is not the same as the projected range R_p. The projected range (R_p) for a single ion is a projection of its range (R) onto its incident trajectory vector. When the beam is normal to the surface (that is, when $\theta = 0°$) projected range (R_p) is equal to the implant depth (X_s) as perpendicular to the target surface [7]. Statistically, the projected range (R_p) is the most used to define depth for an ion implantation.

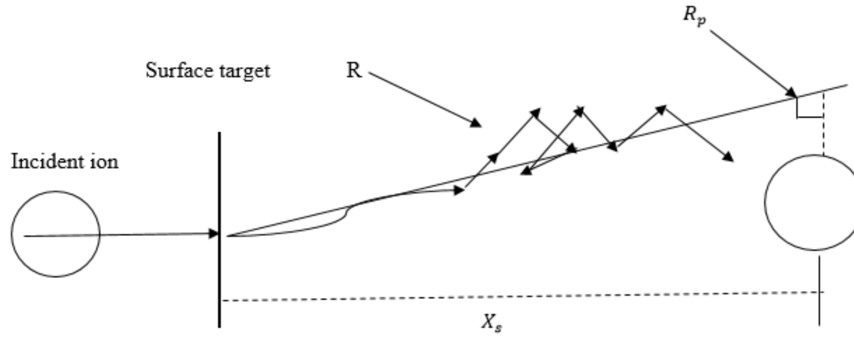

Figure 3.3: *Illustration of the path of a single ion travelling inside a solid target at an angle not equal to the surface normal until it reaches a certain depth within the solid target. Adapted and redrawn from [9].*

Figure 3.3 elaborates the range definition of a single ion penetrating through a material. A collective effect of multiple ions is required by the ion beam process. The range distribution of a large number of ions is statistical in nature. If there is a low concentration of ions implanted, then the probability function describing the distribution is approximately Gaussian and written as [14]:

$$N(x) = \frac{\emptyset}{\sqrt{2\pi\Delta R_p}} e^{-\frac{(x-R_p)^2}{2\pi\Delta R_p{}^2}} \tag{3.15}$$

where $N(x)$ is the ion concentration and $\emptyset$ $\left({}^{ion}/{}_{cm^2}\right)$ is the implanted fluence. The full width at half maximum (FWHM) of the implantation profile can be calculated from the standard deviation that is the range straggle (ΔR_p): $FWHM = 2\left(\Delta R_p\right)\sqrt{2ln2}$ [16]. In this work strontium and silver implanted depth profiles were observed to be near Gaussian. High doses or crystallographic orientation effects can cause the range distribution to deviate from the Gaussian profile. There are many cases that may result the Gaussian profile to be skewed because the ion penetrates to depth that is several times greater than R_p [15].

3.5 Stopping and Range of Ions in Matter (SRIM) for simulation of ion implantation

Stopping and Range of Ions in Matter (SRIM) was created by Ziegler *et al.* [7]. This computer simulation program is based on the Monte Carlo (MC) technique. The MC technique is based on a statistical or random nature of the processes that are modelled. SRIM is technologically advanced for acquiring the ion range, damage range, damage distribution and transmitted ions in amorphous targets. This program treats all targets as amorphous, thereby neglecting the potential contribution of channelling or orientation dependent occurrences to range distributions [18]. It is important to use this program before performing ion implantation experimentally. The MC method gives an idea of what to expect in experimental results. SRIM was done before the implantations in SiC.

When the program is running, certain parameters must be selected, that is, the type of the ion, in this study silver and strontium, the substrate, in this study silicon carbide and the energies of the ions, which are $360\ keV$ and $280\ keV$ in this study. However, SRIM does not account for crystal structure of the material which in some cases limits its usefulness. SRIM makes the following approximations [18,19]:

- Neglect knocked off atoms with the vacancies;
- The target atom sputter if it possesses enough momentum and energy to pass the surface barrier;
- Influence of neighboring atoms is neglected;
- Simulation of materials with composition differences in two dimensions or three dimensions is not possible;
- The electronic stopping power is an averaging fit from a large number of experiments;

References

1. Wikipedia. Ion implantation. [Available on: https://en.m.wikipedia.org/wiki/Ion_implantation]. Accessed on 10 December 2019
2. J. Tesmer, M. Nastasi. Handbook of modern ion beam materials analysis, *Materials Research Society,* Pittsburg, 1995.
3. T. T Thabethe. RBS investigation of diffusion of implanted xenon in 6H-SiC. MSc dissertation, *University of Pretoria.* 2013.
4. G. Was. Fundamental of Radiation Materials Science. Metal and Alloys, *Springer*, Berlin, 2007
5. M. Backman. Effects of nuclear and electronic stopping power on ion irradiation of silicon-based compounds, Academic dissertation*, University of Helsinki*, 2012. [Available online: https://core.ac.uk/download/pdf/14926238.pdf], (Accessed 02 January 2020)
6. M. Mayer. Rutherford Backscattered Spectroscopy (RBS), *Max-Planck-Institut fur Plasmaphysik, EURATOM Association*, Garching, Germany (2003)
7. J. Ziegler, J. Biersack. The stopping and range of ions in matter. *Treatise Heavy-Ion Sci*. (1985) 93–129.
8. J. Lindhard and M. Scharff. Energy loss in matter by fast particles of low charge, *København, I Kommission hos Munksgaard,* 27 (15) (1953) 1–32.
9. J. Ziegler, Ion implantation science and technology. *2nd edition Academic press*, New York. (1988).
10. H. Bethe, Zur Theorie des Durchgangs schneller Korpuskularstrahlen durch Materie. *Annelen der Physik. Leipzig,* 5 (1930) 324.
11. E. Kamaratos. The mean excitation energy for stopping power I, the Bragg rule, and chemical and phase effects. Application of a statistical treatment to the determination of I for chemically bound particles. *Chemical Review.* 84 (1984) 561-576.
12. F. Bloch, Zur Bremsung rasch bewegter Teilchen beim Durchgang durch Materie. *Annalen der Physik.* Leipzig 16 (1933) 285.
13. L. Feldman and J. Meyer, Fundamental of surface and thin film analysis. North-Holland, New York–Amsterdam–London, 1986, 352 Seiten, 175 Abb., 9 Tabellen im Anhang, ca. 150 Literaturzitate. New York. (1987). ISBN 0-444-00989-2

14. N. Bohr, XVIII. The Penetration of Heavy Atomic Particles Through Matter—Introduction: Unpublished Manuscript from Folder Penetration. Niels Bohr Collected Works. 8(1987)403-408
15. L.A. Giannuzz, B.I. Pretnitzer, B.W. Kempshall, Ion-solid interactions FEI Company, Hillsboro, OP 97124, Nanospective Inc. Orlando FL 32826
16. M. Nastasi, J.W. Mayer, J.K. Hirvonen, Ion-solid interactions: Fundamentals and Applications, *Cambridge University Press, Great Britain* (1996)
17. R.J. Kuhudzai, Diffusion and surface effects for SiC implanted with fission product elements. *PhD thesis, University of Pretoria. 2015.*
18. T.T Hlatshwayo, Silver implanted into 6H-SiC. *PhD thesis, University of Pretoria.* 2015
19. J.F. Ziegler. SRIM 2013, www.srim.org, USA,

Chapter 4: Experimental-analysis techniques

The effects of Ag and Sr co-implanted into polycrystalline SiC was investigated using Raman spectroscopy, Rutherford backscattering spectrometry (RBS), and the scanning electron microscopy (SEM). The chapter discussed these techniques.

4.1 Raman spectroscopy

Raman spectroscopy is an analysis technique that irradiates a sample with laser to study the type and state of a substance from the generated Raman scattered light. It analyses the vibrational, rotational and other low-frequency modes of molecules. The Raman spectroscopy has no contact with the sample, it is nondestructive. It analyses the molecular structure, residual stress as well as evaluate crystallinity [1]. In Raman spectroscopy, the sample is irradiated with a strong monochromatic light source, in this study laser light which energize the atoms of the sample. The laser light scatter in all directions. Some of the scattered laser light goes to the detector and the detector records the Raman spectrum [2].

4.1.1 Detection and analysis of inelastic scattered radiation

A typical Raman spectrum of polycrystalline SiC is shown in Figure 4.1.

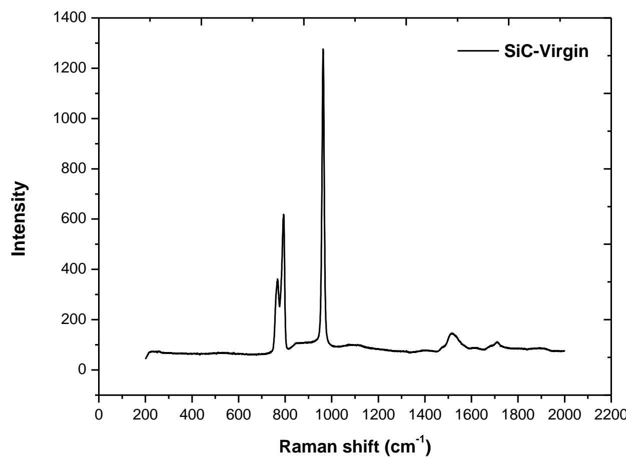

Figure 4.1: *Typical Raman spectrum of virgin SiC obtained in the Raman spectroscopy laboratory at University of Pretoria.*

Particularly, Raman spectroscopy photons interact with a sample of interest by polarizability of those molecules. If light interaction with the molecule it only disrupts the electron cloud and photons will be scattered with small frequency changes due to the small electron mass. When light is dispersed from the sample most of the photons are elastically dispersed. The dispersed photons have [3] equal energies. However, a small fraction of light scattered at optical frequencies exceptional from, and normally lower than the incident photons. This method leading to this inelastic scatter is regarded as the Raman effect [3]. When a photon interacts with the sample different scatterings such as: Rayleigh scattering, Raman-Stoke scattering and Raman- Anti-Stoke scattering are scattered [4].

When incident light interacts with the molecule of the sample an electron in a ground state is energized to a virtual state and then returns to the same state it was before. This is known as Rayleigh scattering. In Stoke scattering the electron begins from a ground vibrational state. It is prompted to a virtual state and then relaxes to an energy state that is higher than the electron's starting state whereas in Anti-Stoke scattering electrons begin in a vibrational state that is more energetic than the ground state. It is excited to the virtual state then decrease back to the ground vibrational state, which is lower in energy than when it started [1,5,6]. This is shown in Figure 4.2.

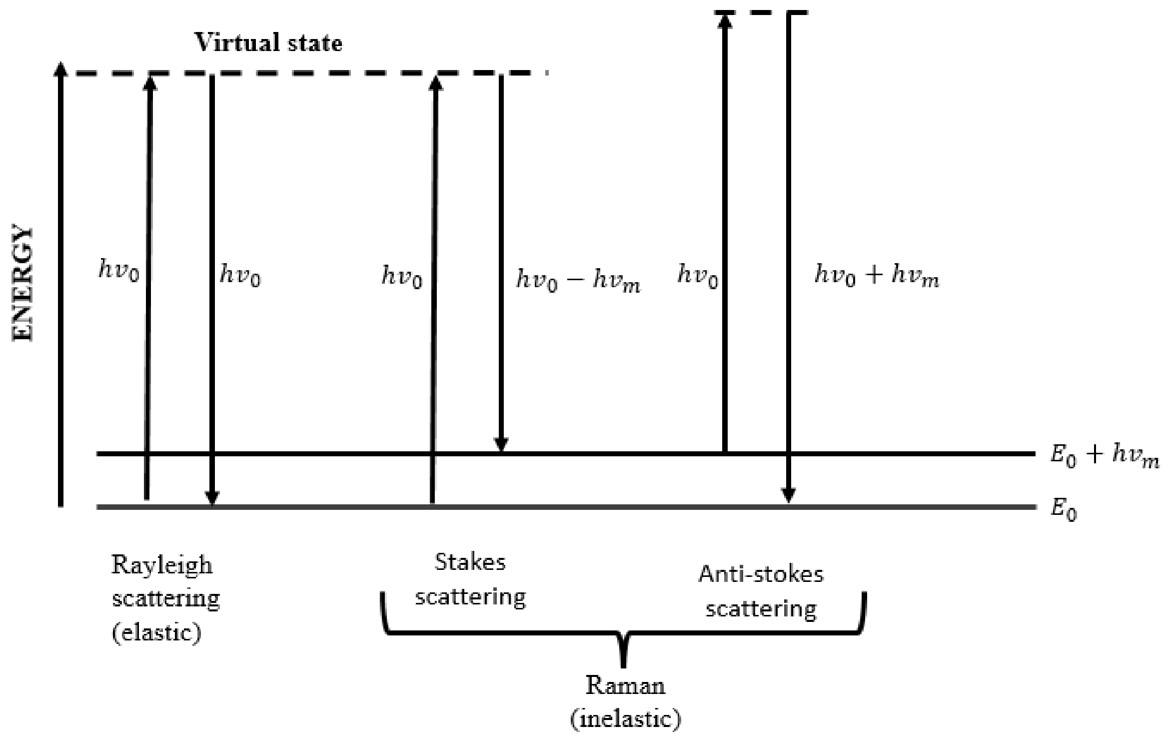

***Figure 4.2**: Diagram of Rayleigh and Raman scattering process. Adapted and redrawn from [7].*

4.1.2 Raman Effect

The Raman effect ascends when a photon is incident on a molecule and interacts with the electric dipole of the molecule [8]. The electric field of the incident light disturbs the charge distribution in the molecule and that is how a dipole moment is created. Raman spectroscopy can be used to discuss the features of the Raman band intensities. Equation (4.1) shows the dipole moment, P, induced in a molecule by an external electric field, E, proportional to the field [8].

$$P = \alpha E \tag{4.1}$$

The proportionality constant α is the molecular polarizability. The induced dipole emits light at the optical frequency of the incident light wave [8]. Raman scattering occurs because a molecular vibration can change the polarizability. This change can be described by the polarizability derivative, $\frac{d\alpha}{dQ}$ where Q represents the normal coordinates of the vibrations. The polarizability is typically different if the field is applied parallel or perpendicular to the molecular axis or in

different directions relative to the molecule. Nonetheless, for a small electric field, the polarizability is the same for the field oriented in opposite directions along the same axis, $(\mu(-E) = -\mu(E))$ [9]. Thus, the distortion induced in a molecule by an applied electric field depends on the relative orientation and returns to its initial value after a rotation of 180 °. The selection rule for a Raman-active polarization requires a change in polarization during the process of vibration $\frac{\partial \alpha}{\partial q} \neq 0$.

An oscillating dipole radiates energy at the frequency of its oscillation. The oscillation of the electric field, E, of the excitation light is given by Equation (4.2)

$$E = E_0 \cos(\omega_0 t) \quad (4.2)$$

Then, Equation (4.1) becomes:

$$P = \alpha E = \alpha E_0 \cos(\omega_q t) \quad (4.3)$$

The molecular polarization usually changes with bond length. The bond length oscillates at the vibrational frequency. Therefore, Equation (4.3) becomes [10]:

$$P = \left[\alpha_0 + \left(\frac{\partial \alpha}{\partial q}\right)_{q_0} q_0 \cos(\omega_q t)\right] E_0 \cos(\omega_0 t) = \alpha_0 E_0 \cos(\omega_o t) + q_0 E_0 \left(\frac{\partial \alpha}{\partial q}\right)_{q_0} \cos(\omega_q t) \cos(\omega_o t) \quad (4.4)$$

Using the identity: $\cos a \cos b = \frac{1}{2}[\cos(a+b) + \cos(a-b)]$.

Equation (4.4) becomes [10]:

$$P = \alpha_0 E_0 \cos(\omega_o t) + \frac{1}{2}\left(\frac{\partial \alpha}{\partial q}\right)_{q_0} q_0 E_0 [\cos(\omega_0 + \omega_q) + \cos(\omega_0 - \omega_q)] \quad (4.5)$$

In Equation (4.5), the first term represents the Rayleigh component, the frequency of the incident light is the same as the frequency of oscillation. The Rayleigh scattering does not give information about the molecular vibration. For the second term it is the Anti-stoke component. It oscillates with the sum of the incident frequency and the frequency of the normal modes. The last term shows the Stokes component. This oscillates with the difference between the incident frequency and molecular normal mode frequency [10].

4.1.3 Raman spectroscopy experimental setup

The experimental setup that was used to collect the data in this work is shown in Figure 4.3. The samples were investigated by a microscope with a confocal configuration. The excitation source was the Argon-Krypton laser at wavelength of $514.5\ nm$ of wavelength. The signal is analyzed by triple monochromator with $1800\ gr/mm$. The analyzed signal was collected by the charged-coupled device (CCD) and converts the signals into electrons and then a signal that can be used in the software. The spatial resolution is about $1\ \mu m$ of diameter for the microscope's objective with apparatus number 0.92.

Figure 4.3: *Image of Raman spectroscopy at the University of Pretoria.*

4.2 Rutherford Backscattering Spectrometry

In 1911, Sir Ernest Rutherford determined the structure of the atom by using the backscattering of alpha particles from a gold film, thereby discovering the atomic nucleus. In 1957, Rubin *et al.* [11] were the first authors to describe the Rutherford backscattering spectrometry (RBS) as a method

for material analysis [11]. RBS is a technique used to analyze near-surface layers of solids. It is mostly used to study thin films, phase change, ion implanted materials, and diffusion. This technique is based on measuring the backscattered beam of energetic ions, in our case, the alpha particles (He^+) from the material of interest. In this study polycrystalline silicon carbide was single- and co-implanted with silver and strontium. The energetic He^+ of 1.6 MeV and /or 1.4 MeV generated by the radio frequency ion source and are accelerated towards the target. The shape of ion beams is controlled by the collimators. The target is settled on the sample holder joined on a 3 pivot goniometer system which features an accuracy of 0.02 ° in each of the angle settings [12]. The secondary electrons may misrepresent the analysis. They are repressed by a -200 V linked to a circular shaped electrode to the fore of the target [12]. Then the solid state detector detects the backscattered ions from the SiC at an angle of 165 ° relative to the direction of incident beam. The detected backscattered ions provide different information about the target. Figure 4.4 shows the diagram of a beam projected towards the target. The RBS is made up of five major components: accelerator (Van de Graaff accelerator in our case), beam line, analysis chamber, detector and the data acquisition setup. These components are discussed below.

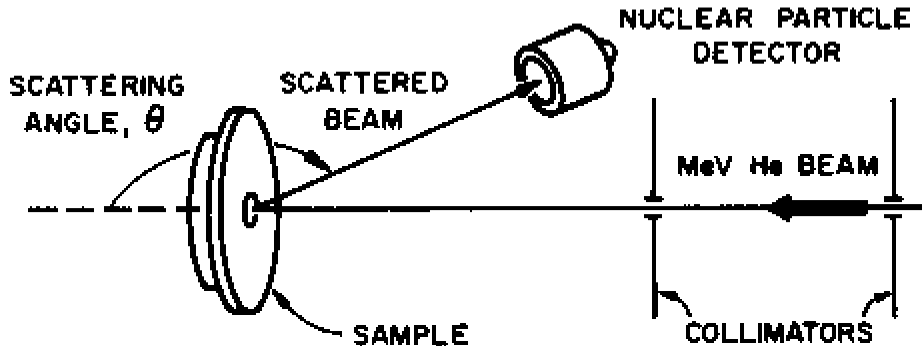

Figure 4.4: *Illustration of an ion beam accelerated towards the material. Taken from [13].*

4.2.1 Components of the Rutherford back scattering spectrometry

A Van de Graaff accelerator is an electrostatic accelerator that is connected to high voltage and low current. It uses a moving belt to mount up charged ions on a hollow metal sphere on top of an insulated column. A typical Van de Graaff accelerator consists of a belt of motor, a lower pulley,

lower electrode, a rubber belt, upper pulley, upper electrode and the hollow metal sphere. The rubber belt is made of a dielectric material running over the lower and upper pulleys. When the motor is turned on the lower pulley begins a negative charge and the belt builds a positive charge at its inner surface while the outside of the rubber belt acquires negative charge by induction. The lower and upper electrodes are in the form of comb-shape rows of sharp metal points. The lower and upper electrodes are best described as the charger comb and collector comb, respectively [14]. They are positioned near the lower pulley and inside the hollow metal sphere. The charger comb drains these negative charges to ground and the positive charges inside the surface of the belt travel upwards. This method of charging is based on the triboelectric effect, wherein simple contact electrification of dissimilar materials become electrically charged after they come into contact with one another and then separate [15]. At the top, rubber belt runs over an upper pulley which picks up these positive charges and retains them. When the negative charges build up on the belt they are carried down to the lower pulley. As the belt keep running charges accumulates on the pulleys. Soon the accumulation of charges reaches ionizing intensity and large numbers of positive and negative charges are generated. Positive charges are transferred to the collected comb and the negative charges are drained to the ground by the charger comb [15]. In this study the charges generated are the He^{+} that was produced by a radio-frequency ion source in the accelerator at University of Pretoria. The maximum voltage of this accelerator used was 2.7 eV and energy of 1.4 MeV and 1.6 MeV was used in this study. The typical Van de Graaff accelerator and the radio-frequency is shown in Figure 4.5.

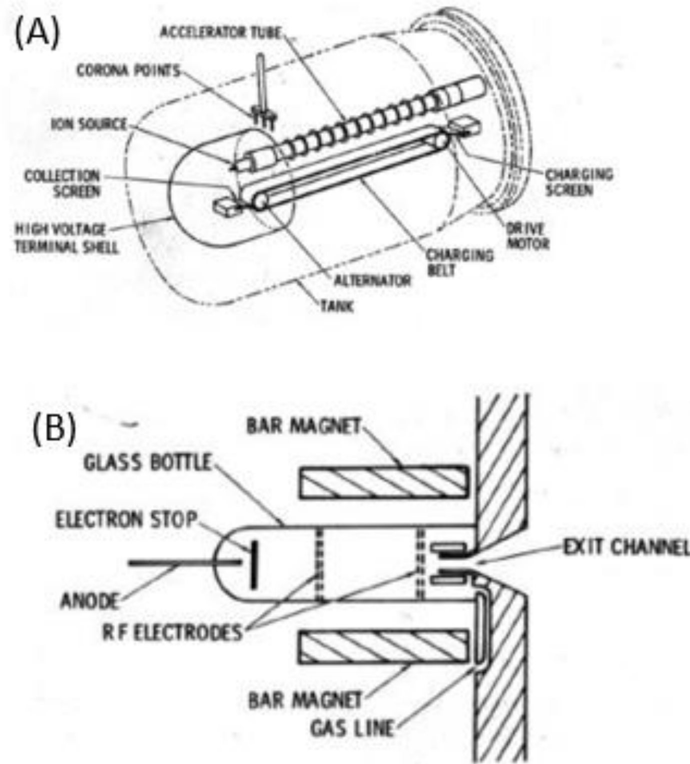

Figure 4.5: *(A) a schematic representation of a Van de Graaff accelerator and (B) radio-frequency ion source. Taken from [16, 24].*

The tube pressure of a Van de Graaff accelerator at University of Pretoria must be kept at about $10^{-8}\ mbar$ so as to diminish interactions amid the accelerated ions and the molecules in the acceleration tube. If ever the pressure in the tube reaches $10^{-4}\ mbar$, voltage breakdown may occur [17].

These high energies of $1.4\ MeV$ and $1.6\ MeV$ were employed to accelerate the He^{+} particles through the beam line. A beam line focuses and guides a beam of high energy He+ into the chamber. During analysis the beam was sustained below the current of $15\ nA$. As the beam of ions is accelerated towards the target, the collimators determine the shape of the beam cross section [17]. The target is placed on a sample-holder inside the analysis chamber. The chamber is then

evacuated to reduce the pressure to $10^{-2}\ mbar$. A turbo pump is utilizing to force down the pressure to $10^{-6}\ mbar$. After measurements the chamber is filled with air at atmospheric pressure.

The backscattered alpha particles were detected by a silicon surface barrier detector operating with a reversed bias voltage of $41.7\ V$. The detector is connected to the pre-amplifier where the backscattered particles are integrated into a voltage. This voltage signal is further amplified by the amplifier and directed to the digital oscilloscope to display the shape of the signal. The amplified signal is then digitalized into a multi-channel analyzer (MCA) whereby the amplified signal is displayed on a computer screen. The RBS spectrum is given by the counts of ions dispersed into the detector as a function of their ion energy [13]. An RBS spectrum of polycrystalline-SiC co-implanted with silver and strontium is visually seen in an xy-plane of counts (y-axis) versus channel number (x-axis). A count is equivalent to concentration and channel is equivalent to backscattered energy. The surface positions of the atoms are clearly seen in the spectrum where an atom with high atomic number will appear in high channel number. A flow diagram of the RBS circuit at the University of Pretoria is shown in Figure 4.6.

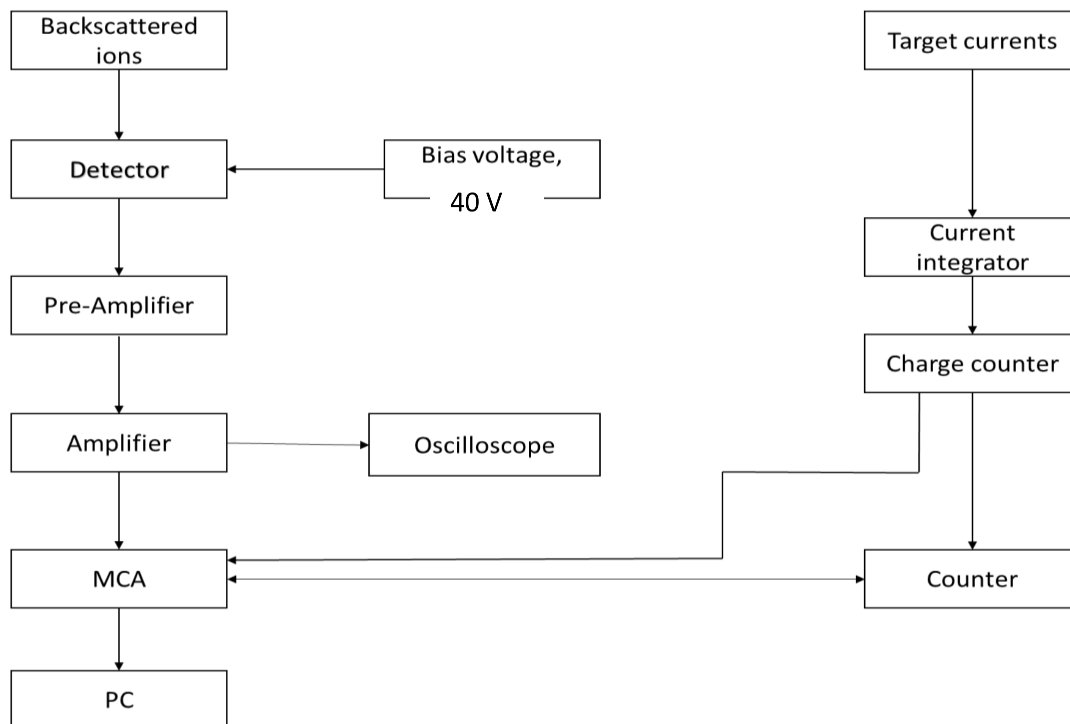

Figure 4.6: *A block diagram for the RBS chamber circuit. Taken from [18].*

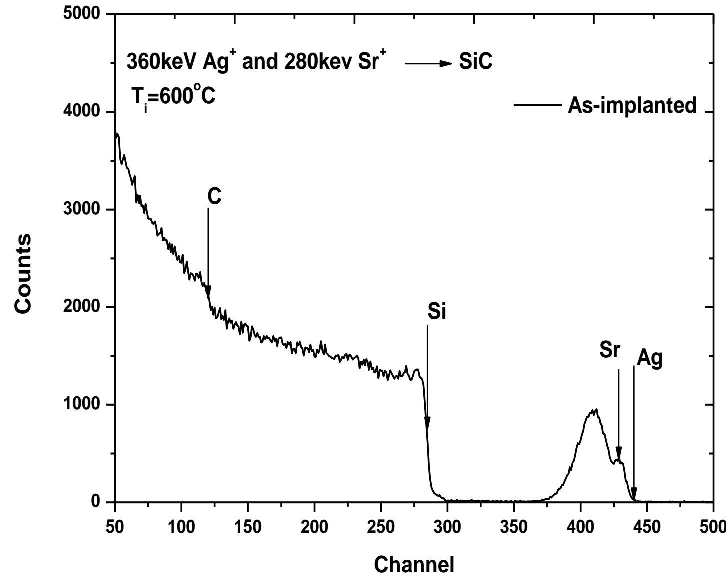

Figure 4.7: *The spectrum of polycrystalline-SiC co-implanted with silver and strontium, with arrows indicate the surface positions of the elements.*

4.2.2 Kinematic Factor

When a collimated energetic beam of ions with mass M_1 and energy E_o impinge on a target, part of the ions are backscattered. The detector is placed at a backscattering angle (165 ° in this study) detects these backscattered ions. In the course of collision energy is transferred from the moving collimated ion beam to targeted atom at rest of mass M_2 [19]. This collision is elastic and follows the principle of conservation of energy and conservation of momentum [19]:

Energy:

$$\frac{1}{2}M_1v^2 = \frac{1}{2}M_1{v^2}_1 + \frac{1}{2}M_2{v^2}_2 \tag{4.6}$$

Momentum:

$$M_1v = M_1v_1 + M_2v_2 \tag{4.7}$$

Conservation of momentum parallel to the incident beam:

$$M_1v = M_1\,v_1\cos\theta + M_2v_2\cos\emptyset \tag{4.8}$$

Conservation of momentum perpendicular to the incident beam:

$$0 = M_1 v_1 \sin\theta - M_2 v_2 \sin\emptyset \tag{4.9}$$

v: velocity of beam particle before collision; v_1: velocity of beam particle after collision; v_2: velocity of target particle after collision; M_1: mass of beam particle; M_2: mass of target particle and θ and $\emptyset$ are scattering and recoil angles respectively. The scattering and the recoil angles are defined as positive numbers with the arrows as shown in Figure 4.8.

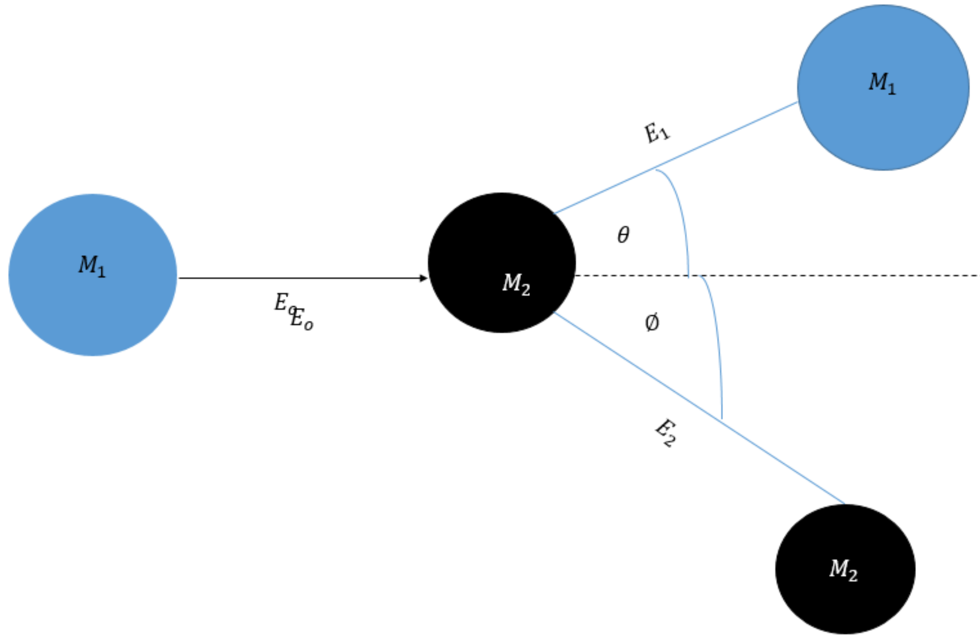

Figure 4.2: *Schematic picture of elastic scattering. M_1 and M_2 are the masses of the incident ion and recoiling atoms, respectively.*

From Equation (4.8) and (4.9), eliminating, $\emptyset$, dependence first, then the momentum of the target,v_2, one finds the ratio of particle velocities that yield the expression:

$$\frac{v_1}{v} = \frac{\pm\sqrt{m^2{}_2 - m^2{}_1 sin^2\theta} + m_1\cos\theta}{m_1 + m_2} \tag{4.10}$$

The energy of projectile (m_1) after collision is found to be the relationship;

$$E_1 = E_0\left[\frac{\pm\left({M_2}^2 - {M_1}^2(\sin\theta)^2\right)^{\frac{1}{2}} + M_1\cos\theta}{M_1 + M_2}\right]^2 \tag{4.11}$$

The ratio of the incident energies for $m_1 < m_2$, where the plus sign holds is:

$$k = \frac{E_1}{E_0} = \left[\frac{\left(M_2{}^2 - M_1{}^2(\sin\theta)^2\right)^{\frac{1}{2}} + M_1\cos\theta}{M_1 + M_2}\right]^2 \quad (4.12)$$

The kinematic factor, k, is the ratio of the energy E_1 to E_0. If $m_1 > m_2$, then negative sign applies. In the current study the summation sign is appropriate because $m_2 > m_1$ and the angle is fixed at $165\,°$ and this equation can be used to calculate the energy $E_1$of the particle backscattered from the known surface element [20].

For this study, backscattering angle was $165\,°$. k has lowest value at $180\,°$ is given by [21]:

$$\frac{E_1}{E_0} = k = \left(\frac{m_2 - m_1}{m_1 + m_2}\right)^2 \quad (4.13)$$

Tabulations of k values for this work are shown in Table 4.1. The k values were calculated using Equation (4.12), where the masses of the targets where $m_{si} = 28, m_c = 12, m_{ag} = 108, m_{sr} = 88$ and the mass of the incident particle is $m_1 = 4$.

Table 4. 1: *Table showing the Kinematic factor k of different target atoms at a scattering angle θ= 165 ° and the backscattered energy.*

$\boldsymbol{E_o}$	$\boldsymbol{k = \left[\frac{\left(M_2{}^2 - M_1{}^2(\sin\theta)^2\right)^{\frac{1}{2}} + M_1\cos\theta}{M_1 + M_2}\right]^2}$	$\boldsymbol{E_1 = kE_0}$
$E_o = 1600\ keV$	$K_{si} = 0.5625$	$E_{si} = 900\ keV$
	$K_c = 0.25$	$E_c = 400\ keV$
	$K_{ag} = 0.8622$	$E_{ag} = 1379.52\ keV$
	$K_{sr} = 0.8336$	$E_{sr} = 1333.76\ keV$

4.2.3 Differential cross section

Assuming an ion beam of number Q ions collide with target type of Q_a. Some particles backscatter from atoms of type a and detected by the detector. This is mathematically given by [22]:

$$Q_a = QN_a\sigma_a d\Omega \quad (4.14)$$

where N_a is the real density of atoms a in the target, σ_a is the differential scattering cross section and $d\Omega$ is the solid angle of the detector. The σ_a determines the odds of a projectile being dispersed by a target atom through an angle θ into a $d\Omega$ placed about θ. If during scattering the interaction between the incident particle and the target atom is the Coulomb potential, then the cross section, σ is given by the Rutherford formula [24]:

$$\frac{d\sigma}{d\Omega} = \sigma(\theta) = \left(\frac{Z_1 Z_2 e^2}{4E}\right)^2 \frac{4\left[\left(m_2{}^2 - m_1{}^2 sin^2\theta\right)^{1/2} + m_2 \cos\theta\right]^2}{m_2 sin^4\theta \left(m_2{}^2 - m_1{}^2 sin^2\theta\right)^{1/2}} \tag{4.15}$$

Experimentally, the number $e^2 = 1.44 \times 10^{-13}\ MeVcm$ is useful, the energy, $E = 1\ MeV$ to $2\ MeV$ He$^+$, is the energy of the projectile immediately before scattering and $\theta = 165\ °$ is the angle of backscattering. Z_1 and Z_2 are the atomic number of the projectile ion mass of m_1 and the atomic number of a target atom of m_2 respectively.

For a compound target, the composition can be calculated using Equation (4.14). For targets containing several elements which might produce overlapping peaks, RBS spectra are analyzed by use of computer simulation, RUMP (Rutherford Universal Manipulation Program) [22].

The incident energies of 1.6 MeV and 1.4 MeV were used together with the corresponding channel numbers of silicon and carbon to perform the energy calibration of the acquired Rutherford backscattering spectroscopy (RBS) spectra.

4.2.4 Depth profiling

When incident alpha particles of energy, E_o impinge the target material, the particles backscatter at different energies and at different depths. Some incident alpha particles backscatter from the target surface having energy, kE_o. Other alpha particles penetrate the target to depth x and backscatter with an initial energy E and then emerges from the surface with energy E_1. These alpha particles that backscatter at depth x have much lower energy than the energy of incidence [24]

The length travelled by the incident alpha particle within the target is [24]:

$$\frac{\Delta x}{\cos\theta_1} = -\int_{E_o}^{E} \frac{dE}{\left(\frac{dE}{dx}\right)} \tag{4.16}$$

and the alpha particles that backscattered at depth x and continuously lose energy when backscattered is given by Equation (4.17) [24]. Figure 4.9 shows the backscattering event of particles and energy loss from a depth of x:

$$\frac{\Delta x}{\cos\theta_2} = -\int_{KE}^{E_1} \frac{dE}{\left(\frac{dE}{dx}\right)} \tag{4.17}$$

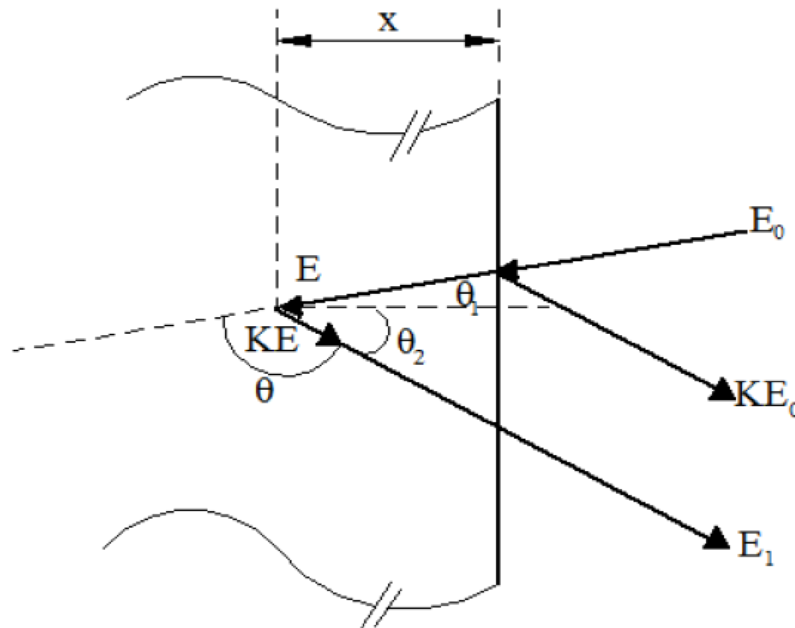

Figure 4.9: *A schematic diagram illustrating the backscattering event of particles and energy loss from depth x. Taken from [16].*

The particles that backscatter at depth x lose their energy when they are penetrating into the target and on the way out of the target after a scattering event. The summation of energy loss of the particles that backscatter at depth x is obtained by presuming the energy loss $\frac{\partial E}{\partial x}$ is constant in both paths the two integrals in Equations (4.16) and (4.17) reduces to [24]:

Inward: $$E = E_o - \frac{x}{\cos\theta_1}\frac{dE}{dx}\Big|_{in} \tag{4.18}$$

Outward: $$E_1 = KE = \frac{x}{\cos\theta_2}\frac{dE}{dx}|_{out} \tag{4.19}$$

The subscripts in and out refer to values of $\frac{dE}{dx}$ along inward and outward paths. Eliminating energy, E, this is done by solving E and equating the Equations: (4.18) and (4.19)

$$KE_o - E_1 = \frac{Kx}{\cos\theta_1}\frac{dE}{dx}|_{in} + \frac{x}{\cos\theta_2}\frac{dE}{dx}|_{out} \tag{4.20}$$

From Figure 4.9 we can see that:

$$KE_o - E_1 = \Delta E = \left[K\frac{dE}{dx}|_{in} + \frac{dE}{dx}|_{out}\frac{1}{\cos(180-\theta)}\right]\Delta x = [\varepsilon]\Delta x \tag{4.21}$$

where, E is the energy of particles backscattered from the atom at depth x [24]. This gives the depth scale that is linear in the energy loss of the alpha particle. Taking ΔE to be the energy difference between the energy of the backscattered particle from the targeted atom at depth x and the energy of the backscattered particle from the surface of the target [24]:

$$\Delta E = KE_o - E_1 = [\varepsilon]x \tag{4.22}$$

Where $[\varepsilon]$ is the energy loss factor. Equation (4.22) becomes:

$$[\varepsilon] = \left[\frac{K}{\cos\theta_1}\frac{dE}{dx}|_{in} + \frac{1}{\cos\theta_2}\frac{dE}{dx}|_{out}\right] \tag{4.23}$$

This stopping cross section factor, $[\varepsilon]$, carries information about the energy and depth information [24]. Also involves the stopping power of the alpha particle in the target. The further the alpha particle travels the more it loses energy in proportion to the penetration depth in the target.

4.3 Scanning electron microscopy (SEM)

Human eyesight has some limit to what man can see. Anything below 0.1 mm to 0.2 mm, the human eye cannot resolve it and requires some sort of magnifying tool. On the basis of producing images above 0.2 mm to the human eye, a microscope was developed and it has a high resolution that is used to study and characterize a wide range of materials. The microscope is divided into two categories, the light microscope and the electron microscope. The dissimilarity in the two microscopes is that one uses visible light while the other uses focused accelerated electron beam [25]. The investigation of the surface changes of the materials can be done using both microscopes.

However, a higher resolution can be attained by using the electron microscopic method because electrons are energetic and have shorter wavelength than visible light [25]. Therefore, by short wavelength the diffraction effects to occur are much smaller which in turn help resolve atomic features ranging from nanometer to micrometer particle size [25]. In this study, SEM was used to characterize the surface evolution of single and co-implanted polycrystalline-SiC. The SEM was introduced first by Von Ardenne in 1938 and by 1965 the first SEM instrument came to market [25].

4.3.2 Fundamental principles of SEM

Behavior in the sample surface after implantation and annealing were examined by SEM. Akhtar *et al.* [25] states that SEM is a versatile advanced instrument which is largely employed to observe the surface marvels of the materials and does not give any internal information about the material [25]. It does this by scanning a specimen with a beam of energetic electrons in an optical column. The electrons emitted by the source shoots the sample with its high energetic electrons and interact with the surface atoms of the specimen and backscattered electrons give information about composition, topography, morphology, orientation of grains and crystallographic information of a material.

When using SEM the samples must be electrically conductive to avoid overcharging on the surface. Overcharging of the sample may lead to poor image and even extreme brightness. Non-conductive samples like polymers are usually coated with a thin layer of a metal to overcome charging [25,26]. The samples are mounted on a stage. The basis for SEM is that it works under vacuum to avoid interaction of the primary electrons with air molecules. If the column was full of gas molecules the electrons could collide with gas molecules and never reach the sample or the gas molecules can react with the sample forming a different compound and condensed on the sample resulting poor quality of the image. Furthermore, the primary electrons emitted from the electron gun at the top are accelerated at $1\ KV$ to $40\ kV$ range [17]. In the current work, the electron high tension (EHT) is the potential which extracts and accelerates the electrons toward the anode.

As soon as the primary electrons hit the sample surface, they interact with near surface atoms of the sample. These electrons have substantial quantities of kinetic energy [25] which is lost inside the sample by generating several signals. The variety of signals emitted when the primary electron

collide with the specimen electrons are; secondary electrons (SEs), backscattered electrons (BSEs), and photons (X-rays) shown in Figure 4.10. These signals are collected by the detectors which are then manipulated by the computer to form an image. Different signals give different information about the sample. SEs and BSEs are mostly used signals to create an image. SEs has much lower energies and indicates sample morphology and topography. They escape from the surface of the sample when some of the energy is transferred from the primary electrons to the specimen's electrons. While the BSEs are referred to as primary electrons that are reflected back from the atomic surface they also have much higher energies than SEs. They are scattered from the sample with little energy loss and are able to travel greater depths with the sample [28]. Their energy is different for every atomic density from which they are reflected. This means that the higher the atomic density the brighter the image will be. They are useful in giving information about orientation and arrangement of the atoms. BSEs are mainly useful for showing phases and composition of any multiphase sample [25]. X-rays are produced by the removal of electrons within an atom. These x-rays are called characteristic x-rays. Characteristic x-rays are produced from the transition of electrons when an electron is knocked out of their shell and an electron from a lower shell must move to higher shell to return the atom to its normal state. Auger electrons are emitted near the surface of the sample. The excitation produced by primary electrons can create inner shell pores. An electron from a higher energy levels fall into a vacancy in an inner shell [28].

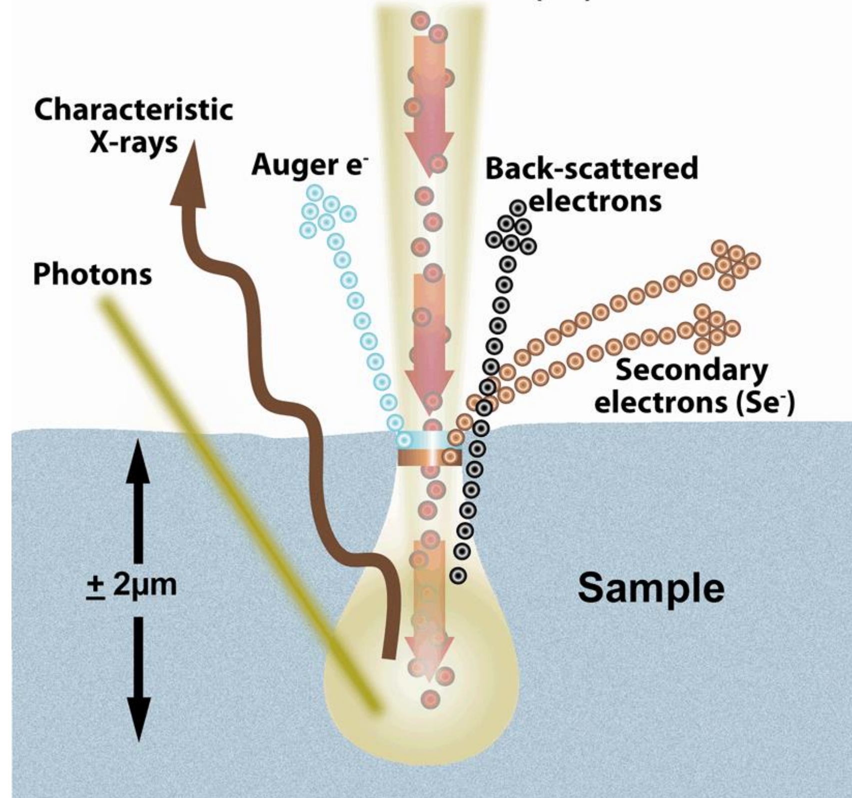

Figure 4.10: *The interaction of electron beam with specimen and the signal emitted from the sample. Taken from [29].*

4.3.3 Instrumentation

SEM consists of the electron gun, vacuum, and column; condenser lens, scanning coil, objective lens, sample holder and detector. First the sample is put on a sample-holder made of copper tape then through the vacuum column.

In the vacuum column there is an electron gun that generates the electron beam. The sample is scanned by the electron beam. Firstly, the gun produces electrons with a metal which is used as a filament for emission of primary electrons. The other function of the electron gun is to provide a stable current in a small beam [25]. There are three types of electron guns [18]: the field emission, tungsten filament and Lanthanum hexaboride (LaB_6). The one used in this study was a field emission gun scanning electron microscope (FEG-SEM). FEG-SEM is also called a cold cathode field emitter which requires an ultra-high vacuum condition to avoid contamination with the anode

below it. The anode has an adjustable voltage from $200\,V$ to $300\,kV$. There is a strong electromagnetic field between the anode and the cathode which accelerates the electron beam towards the condenser lens. The condenser lens is the first lens to focus the electron beam towards the sample [30]. The scanning coils scan the beam of electrons to the sample. The current in the coils can be increased to obtain a higher magnification. For better focusing, objective lens must be at a better working distance ((WD) = distance between the objective lens and the specimen) with the specimen. In this study the WD was in the range of $2.3\,mm$ to $3.3\,mm$. Because our WD is small the sample was at a higher position close to the objective lens. Once the primary electrons hit the sample it produces signals that are mentioned in section 4.3.2. These signals are then detected by the detector (in this study the analysis of the samples used is the inLens-SE detector) and converts the inLens signals to an image that is produced by the computer. The inLens detector is between the scanning coils and the objective lens. Figure 4.11 shows the experimental setup of a typical FEG-SEM and from the University of Pretoria.

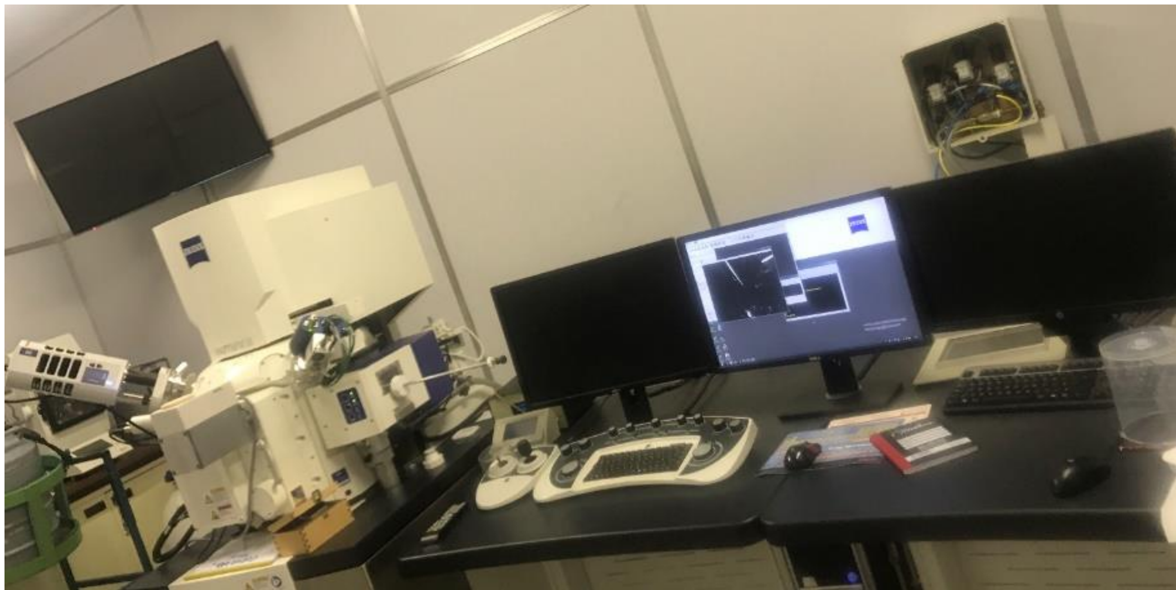

Figure 4.11: *Show the FEG-SEM at the University of Pretoria.*

References

1. Nano photon. What is Raman spectroscopy Available online: https://www.nanophoton.net/raman-spectroscopy/lessons/lesson-2 [Accessed 04 November 2019]
2. Available online: www.nicdetcz.cz/upload/kc/files/aplikacni-podpora/teorie/IntroductionToRaman.pdf [Accessed 19 February 2019]
3. Available online: http://instructor.physics.lsa.umich.edu/adv-labs/Raman_Spectroscopy/Raman_spect.pdf [Accessed 20 February 2019]
4. G. Rajeev. Roman spectroscopy, *Pennsylvania State University*. Available online: https://www.sas.upenn.edu/~lineje/specworkscited.html [Accessed 20 February 2019]
5. Blue Sky and Rayleigh Scattering. *Georgia State University* Available online: https://hyperphysics.phy-astr.gsu.edu/Hbase/atoms/blusky.html [Accessed on 20 February 2019]
6. Department of Materials Science and Metallurgy, *Raman Scattering*. University of Cambridge. Available online: https://www.doitpoms.ac.uk/tlplib/raman/raman_scattering.php [Accessed 20 February 2019]
7. Available online: https://bwtek.com/raman-theory-of-raman-scattering/ [Accessed 20 February 2019]
8. H. A. Vasco, T. T. Hlatshwayo, S.V. Motloung, M. Mlambo, B. S. Mwankemwa, S. Peterovic. Effect of swift heavy ion irradiation in the migration behavior of Xe implanted into TiN. *Vacuum*, 163(2019)59-68
9. T. Dieng, O. Hollricher, J. Toporski, Confocal Raman Spectrometry. *Spring Series in Optical Science*, 158(2010), ISBN:9783642125218.
10. D. Olego, M. Cardona, Pressure dependence of Raman phonons of Ge and 3C-SiC. Physical Review B (USA), 25(1982)151-160
11. S. Rubin, T.O. Passell, E. Bailey, Analytical Chemistry. *Chemical Analysis of Surfaces by Nuclear Methods*, 29 (1957) 736

12. T.T Hlatshwayo. Silver implanted into single 6H-SiC. PhD thesis, *University of Pretoria* (2010)
13. Institute for nuclear and radiation physics. Rutherford backscattering spectroscopy and ion channeling, *Ku Leuven.* Available from: https://fys.kuleuven.be/iks/nvsf/experimental-facilities/rutherford-backscattering-spectrometry-and-ion-channeling [Accessed: 04 Feb 2019].
14. P.G. Mahajan, N.V. Patil, M. S. Shinde. Basic operation and application of Van de Graaff generator, *International Journal of Science Research and Education,* 5(5)(2017)6395-6399. ISSN(e):2321-7545
15. Van der Graaf generator (VDG). Available from: https://physlab.lums.edu.pk/images/d/d8/VDG_final.pdf [Accessed: 04 Feb 2020]
16. R.J. Kuhudzai. Diffusion and surface effects for SiC implanted with fission product elements. PhD thesis. *University of Pretoria* (2015)
17. T. T. Mohlala. Migration behavior of Europium implanted into single crystalline 6H-SiC. MSc dissertation. *University of Pretoria* (2010)
18. T.T. Thabethe. The interfacial reaction and analysis of W thin film on 6H-SiC annealed in vacuum, hydrogen and argon. PhD thesis, *University of Pretoria* (2010)
19. Ernst, F. (2005). *EMSE-515: Rutherford backscattering spectrometry*. [Lecture notes]. Retrieved from: http://www.nuclear.lu.se/fileadmin/nuclear/Undervisning/TillSubFys/RBS-01-Principle.pdf
20. M. Mayer. Rutherford backscattering spectrometry. Max-Planck-Institut f˙ur Plasmaphysik, EURATOM Association, Garching: Germany (2003)
21. T.L. Alford, L.C. Feldman, J.W. Mayer. Fundamentals of nanoscale films. Springer, (2007). ISBN: 978-0-387-29260-1.
22. H. Babet, H. Jenett. Surface and thin film analysis: principles, instrumentation, applications. Wiley-VCH (2002). ISBN: 3-527-30458-4
23. J.R. Tesmer, M. Nastasi, Handbook of modern Ion Beam Materials Analysis. *MRS.,* Pittburg (1995)
24. W.K. Chu, J.W. Mayer, M.A. Nicolet. Backscattering Spectroscopy, Academic Press, New York (1978).

25. Akhtar K., Khan S.A., Khan S.B., Asiri A.M. (2018) Scanning Electron Microscopy: Principle and Applications in Nanomaterials Characterization. In: Sharma S. (eds) Handbook of Materials Characterization. Springer, Cham. https://doi.org/10.1007/978-3-319-92955-2_4
26. G. McMahon Analytical instrumentation: A guide to laboratory, portable and miniaturized instruments. Chichester: Wiley. 1st ed. (2007)296
27. J.I. Goldstein, H. Yakowitz. Practical scanning electron microscopy and x-ray microanalysis. 2nd ed. New York: Plenum Press (1975)
28. W. Zhang, R.P. Apkarian, Z.L. Wang, D. Joy. Fundamentals of Scanning Electron Microscopy. Available from: http://home.ufam.edu.br/berti/nanomateriais/aulas%20pptx%20e%20livros/livro/Scanning%20Microscopy%20for%20Nanotechnology/Fundamentals%20of%20Scanning%20Electron%20Microscopy%20(SEM).pdf [Accessed: 03 Feb 2020]
29. H. Schatten. The role of scanning electron microscopy in cell and molecular biology: In H. Schatten (Ed.), Scanning Electron Microscopy for the Life Sciences (Advances in Microscopy and Microanalysis). Cambridge: Cambridge University Press (2012)1-15 doi:10.1017/CBO9781139018173.002
30. A. Nanakoudis. What is SEM? Scanning electron microscope technology explained. *ThermoFisher SCIENTIFI,* 2019. Available from: https://blog.phenom-world.com/what-is-sem [Accessed: 03 Feb 2020]
31. S.J.B. Reed. Electron microbe Analysis and Scanning Electron Microscopy in Geology. 134(2)(1996)269-281 DOI: https://doi.org/10.1017/S0016756897436464

Chapter 5: Experimental procedure

5.1 Sample preparation

In this study polycrystalline SiC wafers from Valley Designed Corporation were used. The wafers were cut using a diamond scriber into two halves. The implanted SiC samples were cut into $5\ mm \times 5\ mm$ before further treatment. The samples were then cleaned in acetone to get rid of residual that might have contaminated during the process of cutting. The samples were boiled four times for 10 minutes per cycle followed by rinsing them in deionized water. Finally, the samples were dried by nitrogen gas before implantation.

5.2 Implantation

The cleaned SiC samples were sent to Institut für Feskörperphysik, Friedrich-Schiller-Universität, Jena, Germany for implantation. One set of polycrystalline SiC wafers was implanted with $360\ keV$ silver ions to a fluence of $2 \times 10^{16}\ cm^{-2}$ (Ag-SiC) and another set was implanted with $360\ keV$ Sr ions to a fluence of $2 \times 10^{16}\ cm^{-2}$ (Sr-SiC). Some of the Ag-SiC samples were then implanted with Sr ions of $280\ keV$ to a fluence of $2\ \times\ 10^{16}\ cm^{-2}$ (Ag&Sr-SiC). The flux was maintained at rate below $10^{12}\ \ cm^{-2}s^{-1}$.

5.3 Annealing of the samples

The as-implanted samples were annealed from 1000 ℃ to 1400 ℃ for 5 hours in steps of 100 ℃ under vacuum in the order $10^{-5}\ mbar$ using a computer controlled Webb 77 graphite furnace. The samples were placed inside a small glassy carbon crucible before loading into the furnace to avoid contamination. The furnace was then evacuated to a pressure of about $10^{-7}\ mbar$ before annealing. The furnace was cleaned by heating at 100 ℃ for 3 hours. This was also done to make certain that the utmost pressure in the course of annealing was kept at $10^{-5}\ mbar$. The temperature was controlled by a Eurotherm 2704 controller that is connected to a thermocouple and pyrometer. The thermocouple is used to measure temperatures less than 1400 °C and the pyrometer is used to measure temperatures greater or equal to 1400 ℃. The heating rate of 20 ℃$/min$ was used. Once

the annealing was completed the furnace was switched off to let it cool down to room temperature (RT).

5.4 Raman spectroscopy, SEM and RBS measurement conditions

As-implanted and annealed samples were characterized by Raman spectroscopy, scanning electron microscopy (SEM) and Rutherford backscattered spectrometry (RBS). Raman analysis was using a Jobin Yvon, Horiba© T6400 triple Raman spectrometer which uses Ar/Kr laser line of $514.5\ nm$. The spot of $\sim 2\ \mu m^2$ was used to focus the laser beam and collected by a $50\ X$ objective. The morphological changes were monitored by a field emission gun (FEG-SEM) at the University of Pretoria employing a Ziess Ultra 55 with a normal SEM detector and in-lens detector. An accelerating voltage of $2\ kV$ was used. The implanted species were monitored by using RBS after each annealing step using 2 MeV van de Graaff accelerator at the University of Pretoria. The RBS was performed at room temperature using $1.6\ MeV$ of alpha (He) particles. The backscattered particles were detected by a silicon surface barrier detector (with a bias voltage of $41\ keV$) at a backscattering angle of $165\ °$ with respect to incoming beam. The secondary electrons due to beam-target interactions were suppressed by a round-shaped electrode connected to $-200\ V$ in front of the samples holder. The output charge signal of the detector was transmitted into the pre-amplifier. Then it was integrated into a voltage signal. The voltage signal was amplified by the amplifier then digitalized into a multi-channel analyzer (MCA). The amplified signal was displayed on a computer screen as counts as a function of their energy. The beam current was kept at $15\ nA$ to avoid pile-up effect. The incident energies of $1600\ keV$ and $1400\ keV$ were used together with the corresponding channel numbers of silicon and carbon to perform the energy calibration of the acquired RBS spectra. These different energies were used for calibration.

CHAPTER 6: Results and Discussion

In this work, the effect of silver (Ag) and strontium (Sr) ions individually implanted and co-implanted into polycrystalline SiC was investigated. One set of polycrystalline SiC wafers was implanted with 360 keV silver ions to a fluence of $2 \times 10^{16}\ cm^{-2}$ (Ag-SiC) and another set was implanted with 360 keV Sr ions to a fluence of $2 \times 10^{16}\ cm^{-2}$ (Sr-SiC). Some of the Ag-SiC samples were then implanted with Sr ions of 280 keV to a fluence of $2 \times 10^{16}\ cm^{-2}$ (Ag&Sr-SiC). In the co-implanted sample, the ions were sequentially implanted, Ag ions being the first to be implanted then followed by Sr ions. All implantations were performed a 600℃. The as-implanted samples were sequentially annealed at temperatures ranging from 1000 ℃ to 1400 ℃ in steps of 100 ℃ for 5 hours. Structural and morphological changes were investigated by Raman spectroscopy and scanning electron microscopy (SEM), respectively, while the migration behavior of the implanted species was monitored by the Rutherford backscattering spectrometry (RBS). This chapter presents and discusses the findings.

6.1 Simulation results

The simulated depth profiles and displacement per atom (dpa) of Ag-SiC, Sr-SiC and Ag&Sr-SiC obtained using SRIM 2013 [1] are shown in Figure 6.1. The threshold displacement energy 20 eV and 35 eV were used for carbon and silicon sublattices, respectively [2]. The density of 3.21 $g.cm^{-3}$ was used for SiC in the simulations. The fluence was converted into displacement per atom (dpa) using Equation (6.1):

$$dpa = \frac{\left({}^{V_{ac}}/_{ion(cm)} \times 10^{8} \times \varphi(ions.cm^{-2}) \right)}{\rho_{SiC}(ions.cm^{-3})} \qquad (6.1)$$

where, ${}^{V_{ac}}/_{ion(cm)}$ is the vacancy per atom from SRIM 2013, φ is the ion fluence ($2 \times 10^{16}\ cm^{-2}$), and ρ_{SiC} is the theoretical density of silicon carbide ($3.210\ g.cm^{-3} = 9.6419 \times 10^{22}\ atom.cm^{-3}$). Individual implantation of Ag and Sr resulted in dpa of about 40 dpa and 18 dpa on the surfaces and maximum of 64 dpa and 44 dpa at 88 nm in Ag-SiC and Sr-SiC samples respectively. Co-implantation resulted in dpa of about 60 dpa on the surface and a maximum of 110 dpa at the depth of 88 nm in Ag&Sr-SiC samples. From these results, it

is quite clear that more defects are retained on the co-implanted samples. If one assumes a critical amorphization dose of SiC to be 0.3 dpa, both individually implanted and co-implanted SiC will be amorphized [3,4]. However, all implantations were performed at 600 ℃ which is above the critical amorphization temperature of SiC [5]. Therefore, recrystallization in the samples is expected. Furthermore, SRIM predicted the projected range of about 110 nm for the co-implantation, which allows the investigation of the synergistic effect of co-implanted species.

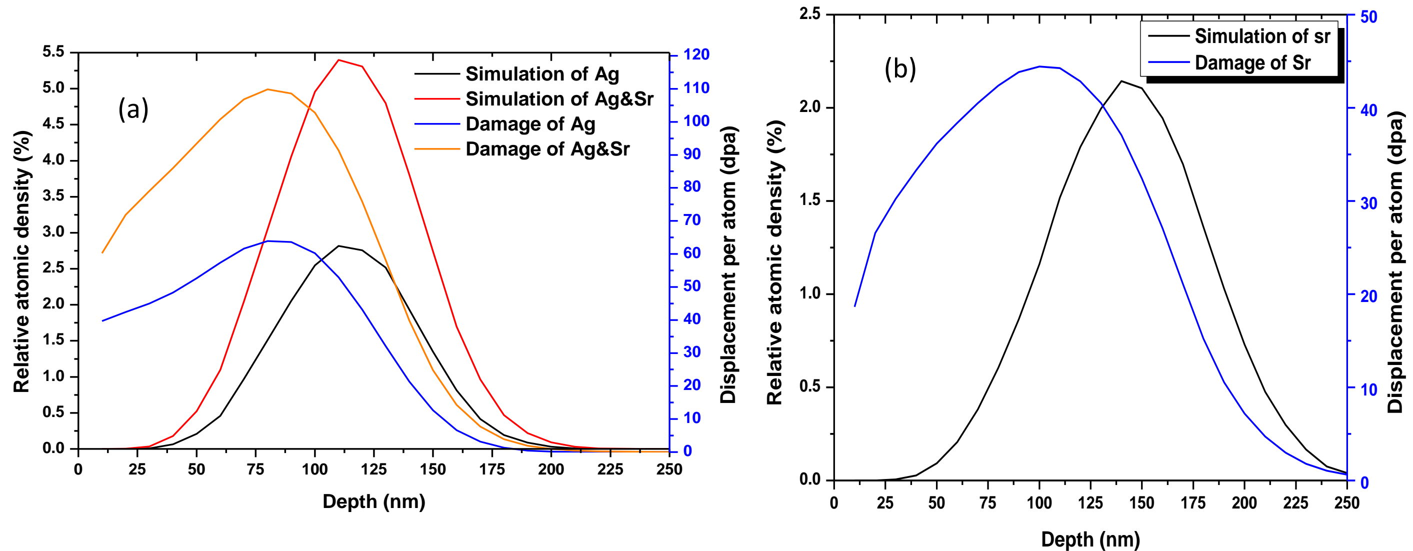

Figure 6.2: *SRIM 2013 simulated depth profiles and displacement per atom (dpa) of (a) Ag (360 keV) & Sr (280keV) and (b) Sr (360 keV) implanted into SiC.*

6.2 Raman results

Figure 6.2 shows the Raman spectra of (a) un-implanted and (b) Ag-SiC, Sr-SiC and Ag&Sr-SiC samples. Un-implanted Raman spectrum has main sharp peaks at 768 cm^{-1}, 797 cm^{-1} and 962 cm^{-1} corresponding to transverse optical (TO) and longitudinal optical (LO) Raman modes of SiC respectively. The broad peaks around 1515 cm^{-1} and 1711 cm^{-1} corresponding to TO overtones are also visible [6-8]. 3C-SiC has Raman peaks at 797 cm^{-1} and 962 cm^{-1} while hexagonal 6H-SiC Raman peaks has at 768 cm^{-1}, 797 cm^{-1} and 962 cm^{-1} [7,8]. Therefore, the present Raman results show TO and LO at 768 cm^{-1}, 797 cm^{-1} and 962 cm^{-1}. This indicates polycrystalline SiC that is composed of both 6H- and 3C-SiC confirming our previous findings

[9], which indicated polycrystalline SiC that was mainly composed of 3C-SiC with some traces of 6H-SiC.

Both individual and co-implantation resulted in the reduction of Raman characteristic peak intensities of SiC accompanied by broadening of LO peak indicating accumulation of defects in SiC as seen in Figure 6.2 (b) and Table 6.1 respectively. The reduction in Raman intensity was more pronounced in the Ag&Sr-SiC samples indicating a higher defect concentration in the co-implanted samples consistent with SRIM predictions. SRIM results indicated higher dpa in the Ag&Sr samples compared to Ag-SiC and Sr-SiC samples. The defects from these two ions might have interacted resulting in the formation of complex defects. Interaction of defects resulting in more complex defects in SiC has been reported in 6H-SiC co-implanted with aluminum (Al) and Carbon (C) at room temperature (RT) [10] and gold (Au) at $600\,K$ and helium (He) at room temperature (RT) [11]. In the study of Wang *et al.* [11] more defects were observed in co-implanted samples compared to single implanted samples. The critical temperature for amorphization of SiC is about $300\,℃$ [5]. Above the critical temperature the SiC remains crystalline with defects. The lack of amorphization in implanted SiC in this study was expected as the implantation temperature was well above the critical temperature of amorphization of SiC [5, 12].

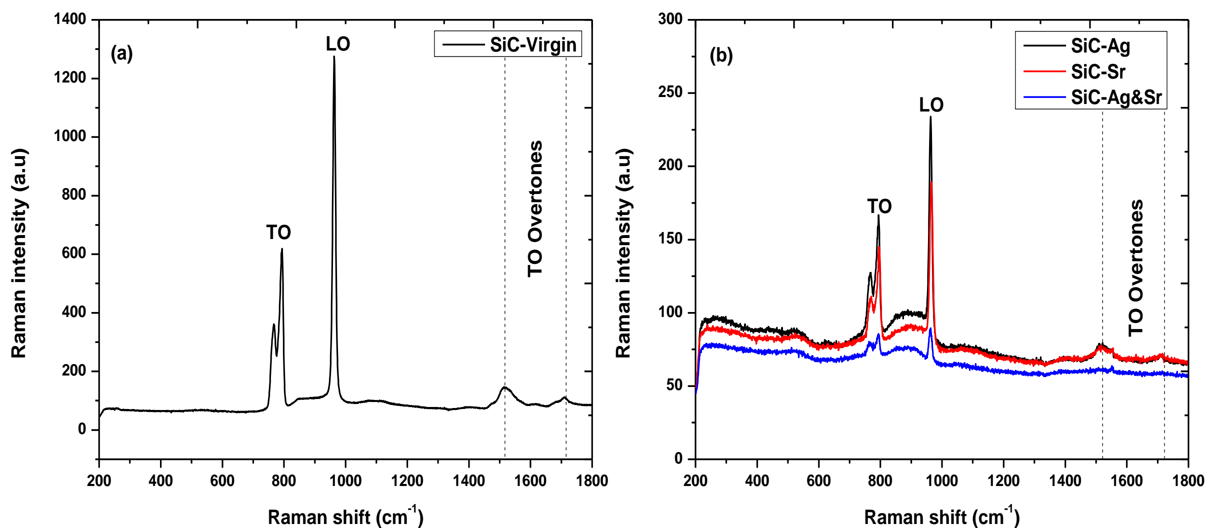

Figure 6.2: *Raman spectra of (a) un-implanted SiC and (b) individual and co-implanted SiC (Ag-SiC, Sr-SiC and Ag&Sr-SiC).*

Table 6.1: *Shows the full with at half maximum of the polycrystalline SiC virgin and as-implanted of Ag-SiC, Sr-SiC and Ag&Sr-SiC.*

Samples	**Full width at half maximum (FWHM)**
Polycrystalline SiC	10.9 cm^{-1}
Ag-SiC (As-implanted)	12.5 cm^{-1}
Sr-SiC (As-implanted)	12.9 cm^{-1}
Ag&Sr-SiC (As-implanted)	13.1 cm^{-1}

Figure 6.3 shows the Raman spectra of Ag-SiC, Sr-SiC and Ag&Sr-SiC before and after sequentially annealing at temperatures ranging from 1000 °C to 1400 °C in steps of 100 °C for 5 hours. While Figure 6.4 show the full width at half maximum (FWHM) of the implants before and after sequential annealing at temperatures ranging from 1000 °C to 1400 °C in steps of 100 °C for 5 hours. Annealing Ag-SiC, Sr-SiC and Ag&Sr-SiC at 1000 °C resulted an increase in the intensities of the Raman characteristic peaks of SiC accompanied by narrowing of LO Raman mode, indicating annealing of defects after annealing at this temperature. This increase in intensities progressed with annealing temperature up to 1400 °C in all samples indicating progressive annealing of defects in the samples. However, this increase in intensities was more pronounced in Ag-SiC and Ag&Sr-SiC samples indicating enhanced annealing of defects in these samples as seen in Table 6.2. The presence of impurities such as Ag and Sr are known to enhance or hinder annealing of defects and crystalline growth in SiC [5,9]. Hence, Ag enhances annealing of defects in the present study. However, the intensities and FWHM of the samples annealed up to 1400 °C are not the same as the ones of virgin sample indicating some defects remaining.

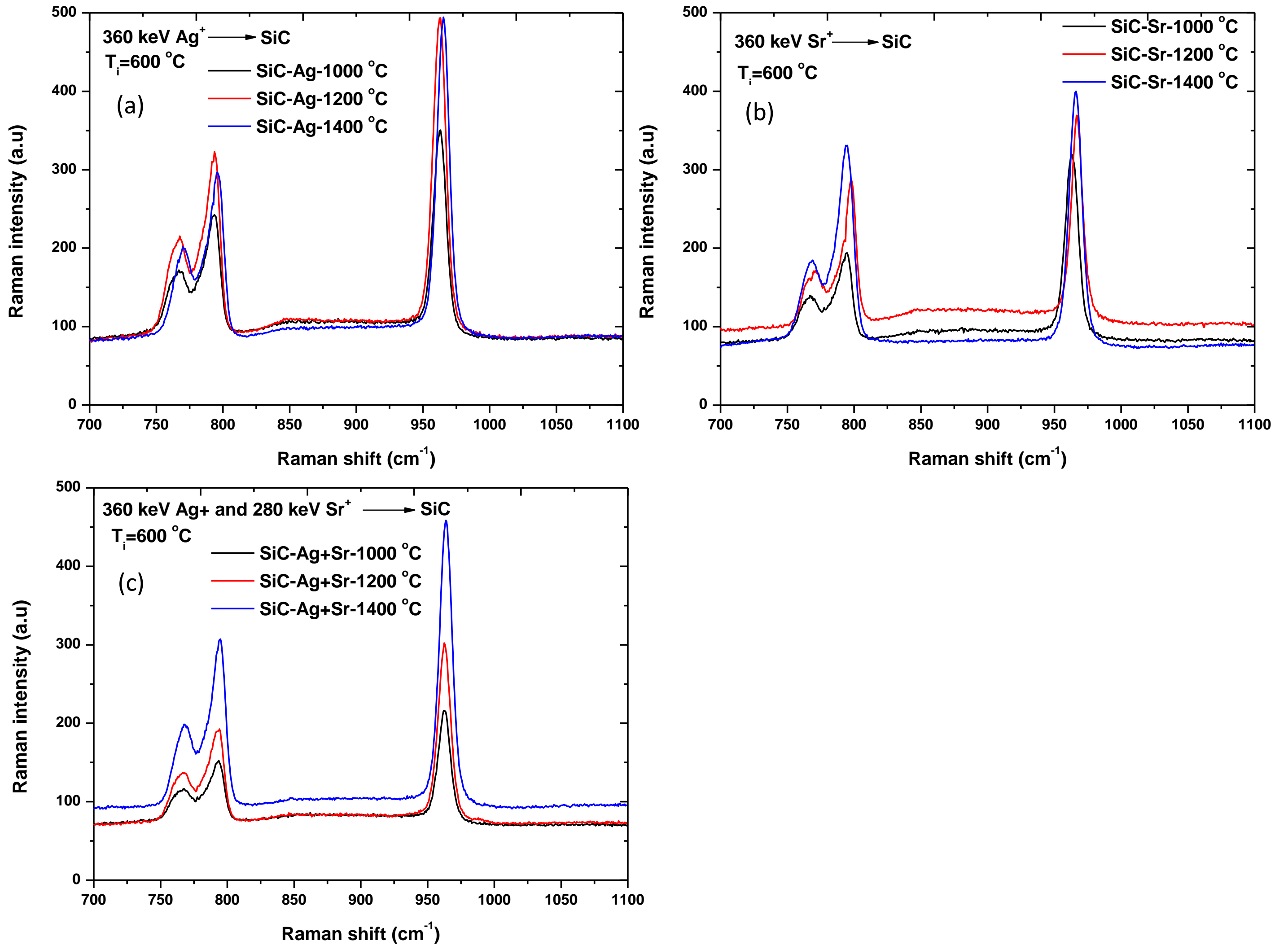

Figure 6.3: *Raman spectra of the annealed (a) Ag-SiC, (b) Sr-SiC and (c) Ag&Sr-SiC at* 1000 °C, 1200 °C *and* 1400 °C.

Table 6.2: *Showing the peak intensities of the annealed samples of Ag-SiC, Sr-SiC and Ag&Sr-SiC at* 1000 °C, 1200 °C and 1400 °C

Annealing temperature	Peak height intensities		
	Ag-SiC	**Sr-SiC**	**Ag&Sr-SiC**
1000 °C	330	325	225
1200 °C	559	376	315
1400 °C	600	425	579

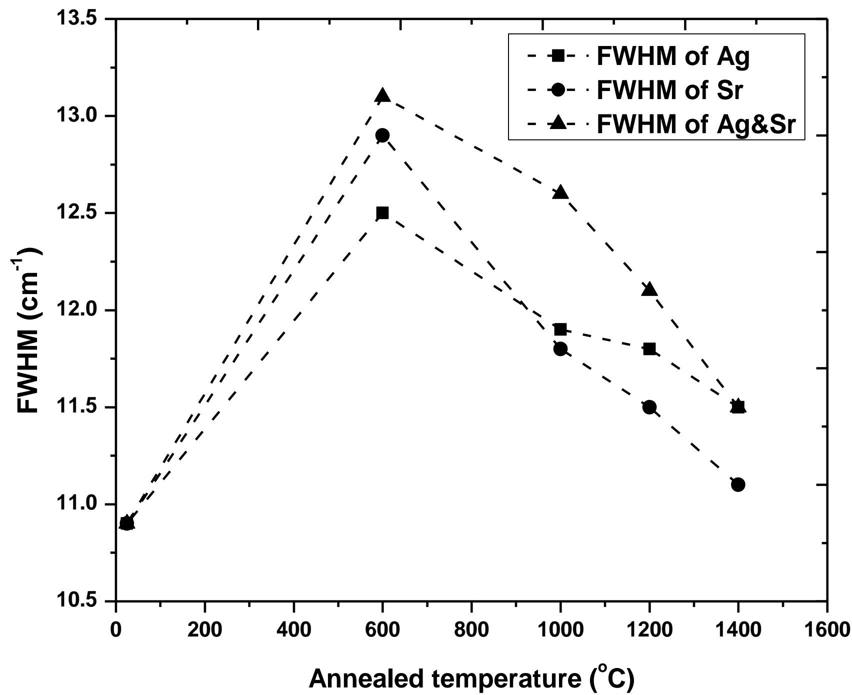

Figure 6.4: *The full width at half maximum (FWHM) of LO mode of Ag-SiC, Sr-SiC and Ag&Sr-SiC as function of annealing temperature.*

6.3 SEM results

Figure 6.5 shows SEM micrographs of the un-implanted, Ag-SiC, Sr-SiC and Ag&Sr-SiC samples. The surfaces of the as-received SiC has polishing marks from manufacturing process. These polishing marks are still visible in all implanted samples confirming the lack of amorphization in agreement with the Raman results discussed earlier. Amorphization is known to cause smoothening of the implanted SiC surface due to swelling leading to the disappearance of the polish marks [13]. Hence the appearance of polishing marks indicates lack of amorphization consistent with Raman results.

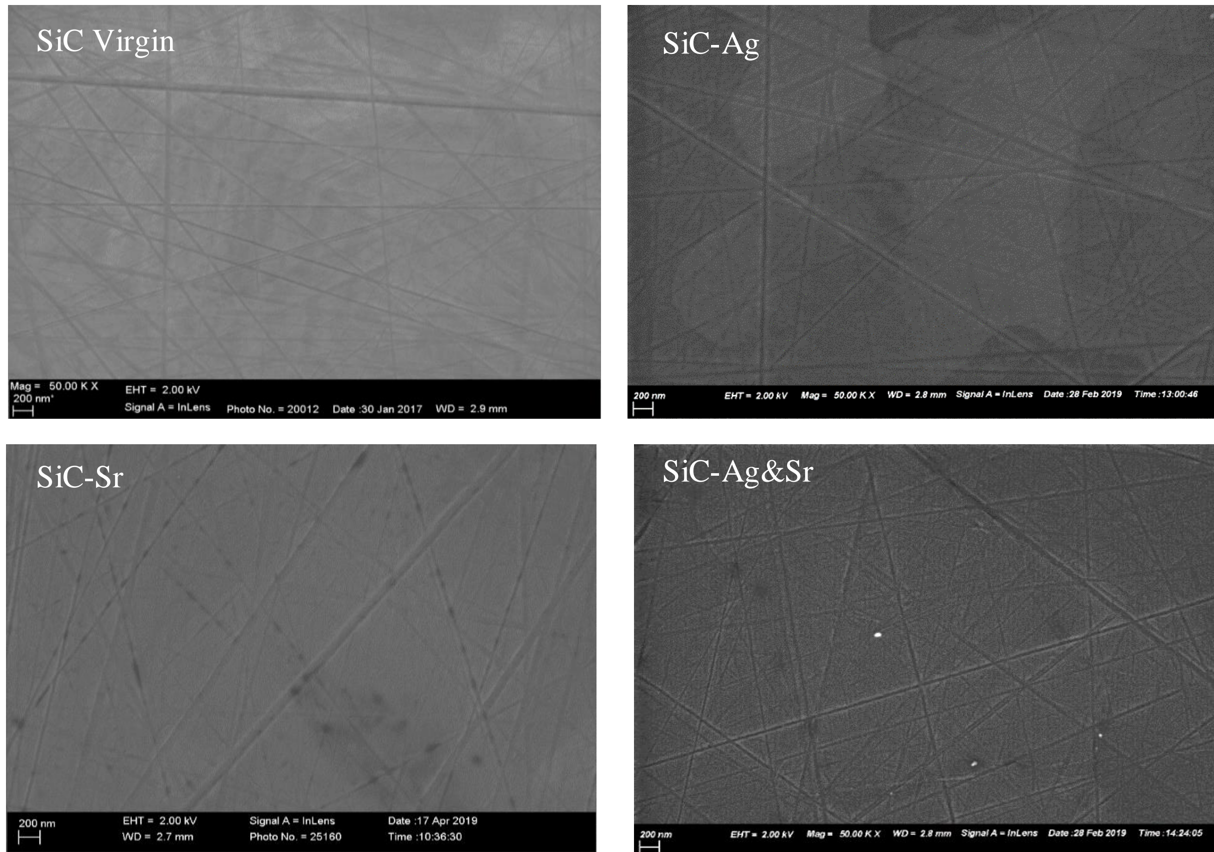

Figure 6.5: *SEM micrographs of as-received SiC, Ag-SiC, Sr-SiC and Ag&Sr-SiC samples.*

Figure 6.6 shows the SEM micrographs of the annealed implanted samples. High magnification micrographs are shown as inserts in Figure 6.6. Annealing Ag-SiC, Sr-SiC and Ag&Sr-SiC samples at 1000℃ caused slight appearance of grain boundaries with polishing marks still present indicating some recrystallization. The appearance of grain boundaries became more pronounced with increasing annealing temperature. Annealing the Ag-SiC, Sr-SiC and Ag&Sr-SiC samples at 1400℃ resulted in rough surface accompanied by crystallites protruding on the surface that is surrounded by pores. The Sr-SiC samples had few pores

that are not connected while Ag-SiC samples had large pores that are connected. From these results, it is quite clear that the presence of implanted Sr in the Ag&Sr-SiC samples acts as an impurity hindering crystal growth leading to small crystallites and small pores in the SiC crystalline. Whereas the interaction of the implanted Ag with SiC led to pores. Hlatshwayo *et al.*

[13] reported that annealing the room temperature (RT) Ag implanted 6H-SiC at temperatures above 1200 ℃ caused interactions of Ag with SiC resulting in deeper pores that provides a pathway for Ag migration [13].

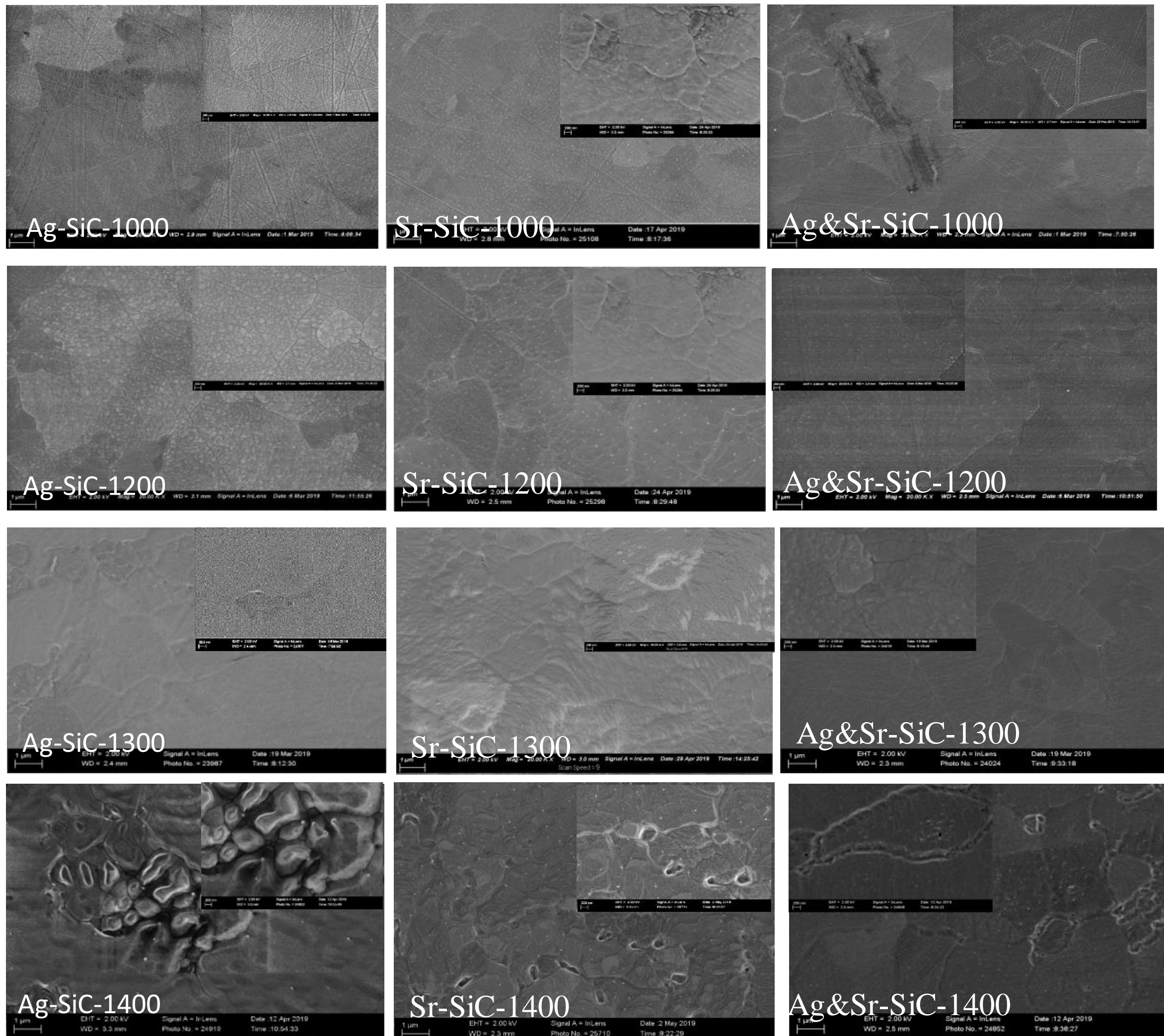

Figure 6.6: *SEM micrographs of Ag-SiC, Sr-SiC and Ag&Sr-SiC sequentially annealed from* $1000 - 1400$℃ *in steps of* 100℃ *for 5 hours.*

6.4 RBS results

The migration behaviour of implanted species was monitored by RBS after each annealing step. Figure 6.7 shows the RBS spectra of the as-implanted samples. The arrows indicate the surface

position energy in channel numbers. The RBS profiles of implants before and after sequential annealing from 1000 °C to 1400 °C are shown in Figure 6.8. Their retained ratios and peak positions as a function of annealing temperature are shown in Figure 6.9.

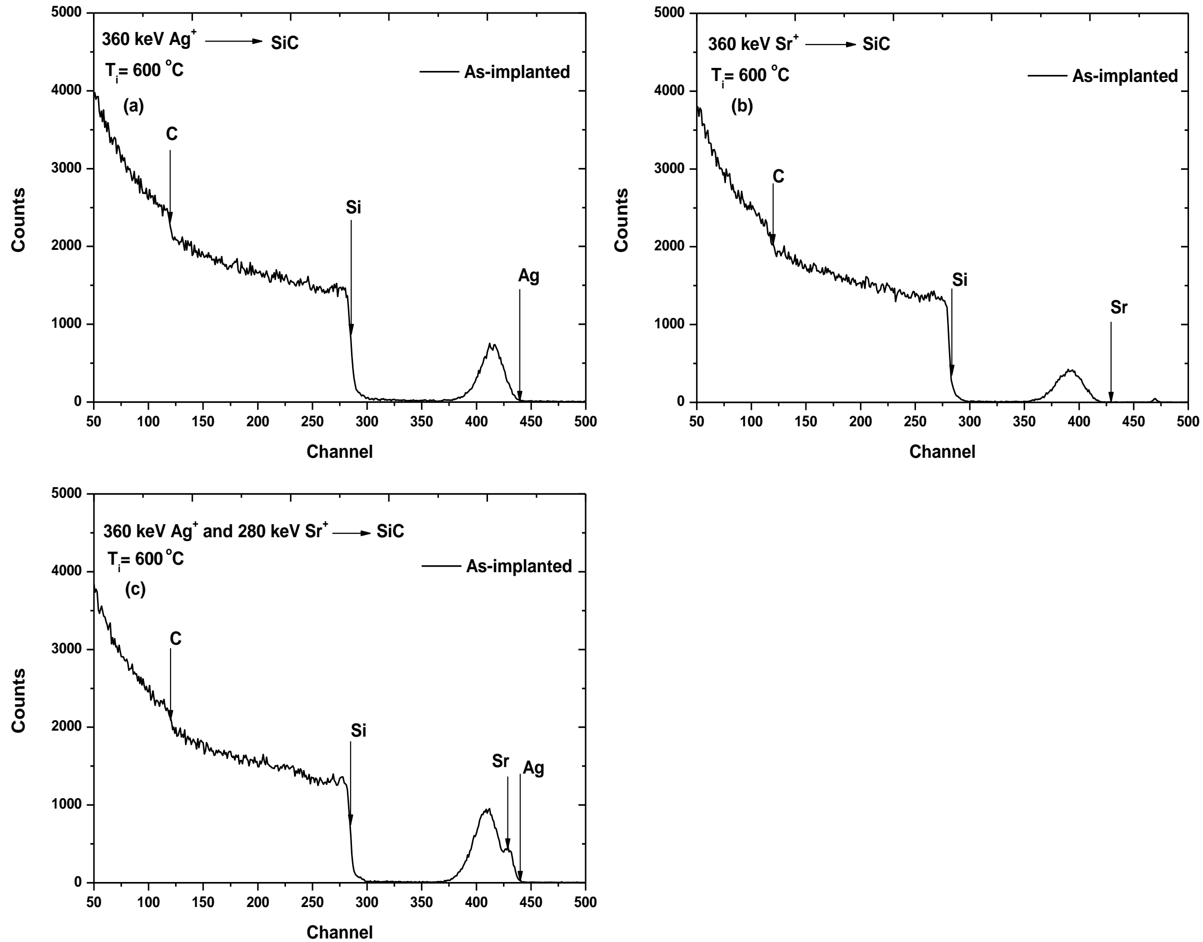

Figure 6.7: *Rutherford backscattering spectrometry spectra of (a) Ag-SiC, (b) Sr-SiC, and (c) Ag&Sr-SiC. The arrows indicate the surface position of elements.*

The as-implanted Ag and Sr profiles of Ag-SiC and Sr-SiC samples are Gaussian distribution as expected for implanted species [14], while the profiles of implants in Ag&Sr-SiC is bimodal distribution. The bimodal profile was found to be due to Ag diffusion and forming precipitates during Sr implantation [9]. Formation of Ag precipitates in Ag implanted SiC at room temperature (RT) after annealing at 900 °C and 1250 °C was observed by Hlatshwayo *et al.* [15] and for other implanted species [16]. In the current study, silver precipitates are observed at implantation

temperature not in annealing temperatures indicating radiation-enhanced silver diffusion during Sr implantation.

Annealing the Ag-SiC and Ag&Sr-SiC samples at 1000 ℃ and 1100 ℃ caused no change in the profiles, while the Sr profile shifted towards the surface after annealing the Sr-SiC samples at 1100 ℃. The shift towards the surface of Sr in the Sr-SiC progressed with annealing temperature up to 1400 ℃ as it can been in Figure 6.9 (b). No loss of implanted Sr was observed after annealing up to 1400 ℃ as seen in Figure 6.9 (a). Ag in the Ag-SiC samples and profile of the implants in Ag&Sr-SiC started to shift towards the surface after annealing at 1200 ℃ as seen in Figure 6.9 (b). These shifts of implants in Ag-SiC and Ag&Sr-SiC were accompanied by loss after annealing at temperatures above 1300 ℃. About 60 % of implanted Ag in Ag-SiC was lost, about 20 % of implants was lost in the Ag&Sr-SiC after annealing at 1400 ℃ as can be seen in Figure 6.9 (a). Comparing these results, it is quite clear that Ag has a role to play in the loss of the implants in Ag&Sr-SiC. SEM micrographs of Ag-SiC showed that Ag interactions with SiC results in wider pores than in the Sr-SiC samples which resulted in the Ag&Sr-SiC samples to have few pores. This means that Ag in Ag-SiC and Ag&Sr-SiC samples has the influence in the formation of pores that act as a migration pathway of the implants.

These are important results in nuclear reactors where SiC is used as the main barrier of fission products. These findings add knowledge on the co-existing fission products in the nuclear core that Ag plays the role of opening pores in the SiC for the migration of other fission products like Sr.

Figure 6.8: *(a) Ag-SiC, (b) Sr-SiC and (c) Ag&Sr-SiC. The as-implanted and then sequential annealed from* 1000 ℃ *to* 1400 ℃ *in steps of* 100 ℃ *for 5 hours.*

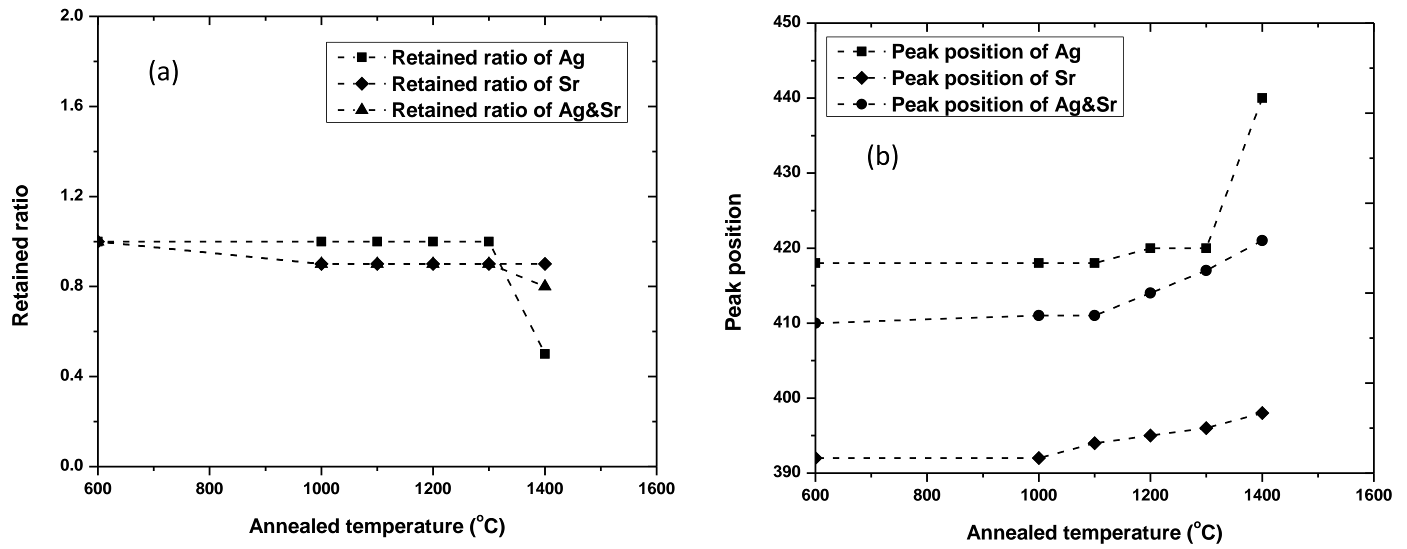

Figure 6.9: *(a) Retained ratio and (b) peak position of implants of Ag-SiC, Sr-SiC and Ag&Sr-SiC samples before and after sequential annealing at temperatures from* 1000 ℃ *to* 1400 ℃ *in steps of* 100 ℃ *for 5 hours.*

References

1. J.F. Ziegler, M.D. Ziegler, J.P. Biersack. SRIM-The stopping and range of ionsing matter, *Nuclear Instrumental Methods Physics Research B: Beam Interactions with Material and Atoms,* 268 (2010) (11-12)1818-1823

2. F. Gao, W.J. Weber, Cascade overlap and amorphization in 3C-SiC: defect accumulation, topological features, and disordering, *Physica Review B Condensed of Matter* 66 (2) (2002) 1–10

3. W.J. Weber, N.J. Hess, L.M. Wang, N. Yu. Structure and properties of ion-beam-modified (6H) silicon carbide, *Materials Science and Engineering. 29* (49)(1998)62-70
4. C.J. McHargue, J.M. Williams, Ion implantation effects in silicon carbide, *Nuclear Instruments and Methods in Physics Research Section B: Beam Interactions with Materials and Atoms,* 80(1993)889-891

5. J.B. Malherbe. Diffusion of fission products and radiation damage in SiC. *Journal of Physics D: Applied Physics*, 46(7)(2013)
6. S. Nakashima, H. Harima. Raman investigation of SiC polytypes, *Physica Status Solidi C* 162 (1997) 39–64.
7. R. Devanathan, W.J. Weber, F. Gao, Atomic scale simulation of defect production in irradiated 3C-SiC. *Journal of Applied Phys*ics 90 (5) (2001) 2303–2309.
8. Z.A.Y. Abdalla, M.Y.A. Ismail, E.G. Njoroge, T.T. Hlatshwayo, E. Wendler, J.B. Malherbe, Migration behaviour of selenium implanted into polycrystalline 3C–SiC. *Vacuum* 175 (2020) 109235
9. T.T. Hlatshwayo, N.Mtshonisi, E.G. Njoronge, M. Mlambo, M. Msimanga, V.A. Skuratov, J.H.O'Connell, J.B. Malherbe, S.V Motloung. Effect of Ag and Sr dual implanted into SiC, *Nuclear Instrument and Methods in Physics Research B,* 472 (2020) 7-13
10. T. Ohshima, A. Uedono, H. Abe, Z. Chen, H. Itoh, Y. Masahito, K. Abe, O. Eryu, K. Nakashima. Positron annihilation study of vacancy-type defects with aluminum and carbon ions. *Physica B-condensed Matter – PHYSICAL B. 308*(2001)652-655 DOI: 10.1016/S0921-4526(01)00780-3.

11. X. Wang, Z. Zha, M. Zhang, Y. Zhao, D. Han, J. Chu, Y. Sun, H. Wang, S. Liu. Damage effects of Au&He dual ion irradiated silicon carbide, *Material Research Express,* 5(2018)10
12. W. Wesch, A. Heft, J. Heidl, H.P. Strunk, T. Bachmann, E. Glaser, E. Wendler. Investigation of radiation damage in ion implanted and annealed SiC layers, *Nuclear Instruments and Methods in Physics Research Section B: Beam Interactions with Materials and Atoms,* 106(1-4)(1995) 339-345
13. J.B. Malherbe, N.G. van der Berg, A.J. Botha, E. Friedland, T.T. Hlatshwayo, R.J. Kuhudzai, E. Wedler, W. Wesch, P. Chakraborty, E.P. da Silveira. SEM analysis of ion implanted SiC. *Nuclear Instruments and Method in Physics Research B*, 315 (2013) 136-141
14. J.B. Malherbe, P.A. Selyshchev, O.S. Odutemowo, C.C. Theron, E.G. Njoroge, D.F. Langa, T.T. Hlatshwayo, Diffusion of a mono-energetic implanted species with a Gaussian profile, *Nuclear Instrumants and Methods in Physics Research B* 406 (2017) 708-713
15. T.T. Hlatshwayo, J.B. Malherbe, N.G. van der Berg, L.C. Prinsloo, A.J. Botha, E. Wendler, W. Wesch. Annealing of silver implanted 6H-SiC and diffusion of the silver. *Nuclear Instruments and Method in Physics Research B* 274(2012) 120-125.
16. W. Jiang, Y. Zhang, W.J. Weber. Temperature dependence of disorder accumulation and amorphization in Au-ion irradiated 6H-SiC. *Physical Review B,* 70(16) (2004), 165208

Chapter 7: Conclusion and future work

The current study, effects of Ag and Sr ions individually and co-implanted into SiC at 600 ℃ was probed. Ag ions of $360\ keV$ and Sr ions of $280\ keV$ were co-implanted into polycrystalline SiC, all to a fluence of $2 \times 10^{16}\ cm^{-2}$ at 600 ℃. For comparison, Ag ions of $360\ keV$ and Sr ions of $360\ keV$ were also separately implanted into polycrystalline SiC, both to a fluence of $2 \times 10^{16}\ cm^{-2}$ at 600℃. Implanted samples were isochronally annealed at temperatures varying from 1000 ℃ − 1400 ℃ in steps of 100 ℃ for 5 hours.

Raman spectroscopy results displayed a decrease in intensities of SiC Raman characteristic peaks indicating accumulation of defects without amorphization in all implanted samples. More defects were retained in the co-implanted samples. The lack of amorphization in the implanted samples SiC was expected as the implantations were performed at a temperature well above the critical amorphization temperature of SiC. While more defects in the co-implanted samples were due to interaction of defects resulting in the formation of more complex defects. Annealing the implanted samples resulted in an increase in the characteristic SiC Raman peaks intensity that progressed with elevating annealing temperature indicating the progressive annealing of defects. However, the intensities of annealed samples were still lower than those of the virgin SiC sample indicating some defects remained. Annealing of defects was observed in the Ag-SiC and Ag&Sr-SiC indicating the effect of Ag on the recrystallization. SEM micrographs of the as-implanted samples had polishing marks indicating lack of amorphization in agreement with the Raman results. The annealed SEM micrographs showed that Sr inhibits crystal growth while Ag creates pathways for the implanted species to migrate to the surface.

RBS results indicated the formation of Ag precipitates in the co-implanted samples due to irradiation induced diffusion during Sr implantation. Annealing resulted in the loss of implants in Ag-SiC and Ag&Sr-SiC at temperatures above 1300 ℃ pointing to Ag as a role player in the loss of the implants. This loss was found to be due to Ag interacting with SiC resulting in the formation of pores that act as migration path for implants.

These are important results in nuclear reactors where SiC is used as the main barrier of fission products. In such environment, the role of Ag in the migration of another fission product need to be taken into consideration. However, in a nuclear reactor different fission products interact with

SiC. In the present study Ag was implanted first followed by Sr. In future it could be interesting to consider a case were Sr will be implanted first then followed by Ag. This mechanism could for instance aid to improve the formation of pores in SiC. Finally, similar investigation will be performed at an atomic level using atomic probe tomography (APT), secondary ion mass spectrometry (SIMS) and X-ray photoelectron spectrometry (XPS).to get more insight of chemical identities, chemical state and composition of the solid surface and near the surface of the sample.

Chapter 8: Appendix

The work presented in this dissertation has made to publications and conference presentations. A synopsis of the outputs is listed in section 8.1 and 8.2.

8.1 A publication in peer reviewed journal

T.T. Hlatshwayo, **N. Mtshonisi**, E.G.Njoroge, M.Mlambo, M. Msimanga, V.A. Skuratov, J. H.O'Connell, J.B. Malherbe, S.V. Motloung," Effects of Ag and Sr dual ions implanted into SiC" Nuclear Inst. and Methods in Physics Research, B 472 (2020) 7

Effects of Ag and Sr dual ions implanted into SiC

T.T. Hlatshwayo [a], N. Mtshonisi [a], E.G. Njoroge [a], M. Mlambo [a], M. Msimanga [b], V.A. Skuratov [c, d, e], J. H.O'Connell [f], J.B. Malherbe [a], S.V. Motloung [g, h]

8.2 Conference presentation

The results of this work were presented Radiation effects in Insulators-20 (REI 20), NUR-SULTAN 2019.

Thulani Hlatshwayo, **N. Mtshonisi**, E. Wendler, E.G. Njoroge, M. Mlambo, J.B. Malherbe, Effect of strontium in the migration of silver implanted into SiC, 20th International conference of radiation effects in insulators, 19-23 August 2019, Astana, Kazakhstan, (Poster presentation)